Macromolecules
Article
pubs.acs.org/Macromolecules

Molecular Origins of Macroscopic Mechanical Properties of Elastomeric Organosiloxane Foams

R. J. Messinger,[†] T. G. Marks,[‡] S. S. Gleiman,[§] F. Milstein,[‡] and B. F. Chmelka*,[†]

[†]Department of Chemical Engineering and [‡]Department of Mechanical Engineering, University of California, Santa Barbara, Santa Barbara, California 93106, United States

[§]Institute of Multiscale Materials Studies, Los Alamos National Laboratory, Los Alamos, New Mexico 87544, United States

S *Supporting Information*

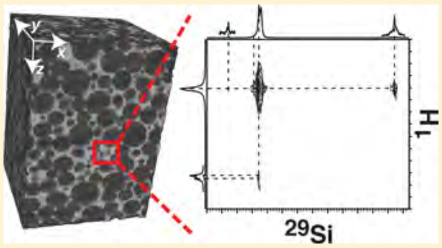

ABSTRACT: Molecular compositions, structures, interactions, polymer chain dynamics, and micron-scale cell structures of elastomeric organosiloxane foams have been analyzed and correlated with their macroscopic mechanical properties. Open-cell organosiloxane foams were synthesized within a narrow range of relative densities (±5% relative uncertainty) and with similar micron-scale pore structures, as determined from quantitative analyses of micro-X-ray computed tomography (MXCT) images. Network cross-linking densities, polymer molecular weights, organic side-chain moieties, and inorganic filler contents were varied systematically, resulting in materials with significantly different mechanical properties. Solid-state single-pulse ^{1}H and ^{29}Si magic-angle-spinning (MAS), two-dimensional (2D) ^{29}Si{^{1}H} hetereonuclear correlation (HETCOR), and transverse ^{1}H relaxation (T_2) nuclear magnetic resonance (NMR) spectroscopy measurements establish significant differences in molecular and polymer network characteristics that are correlated with the bulk mechanical properties of the organosiloxane foams. These characteristics include differing extents of polymer cross-linking, concentrations of phenyl side-chain groups, mass fractions of low- to high-molecular-weight cross-linking chains, and polymer chain dynamics. The mechanical properties of the organosiloxane foams are accounted for by the differences in the molecular compositions, structures, and polymer chain dynamics of the foam frameworks, independent of cell microstructures.

■ INTRODUCTION

Polymeric cellular solids are designed and manufactured on large scales for their superior mechanical, insulation, and/or energy storage properties with respect to their weights and raw material costs.[1−4] In particular, open-cell elastomeric foams (e.g., macroporous siloxanes) are ubiquitous in diverse aerospace, automotive, construction, and packaging applications,[1] which require significantly different mechanical properties. The origins of such differences are complicated and not well understood, in part because solids that are both elastomeric and cellular possess both molecular and micron-/macroscale structural features that influence their bulk mechanical responses and that are challenging to disentangle. To do so, it is desirable to establish the relative influences that specific molecular characteristics and cell microstructures have on the macroscopic mechanical properties of elastomeric foam materials.

For cellular solids, extensive research has been conducted on cell structure−property relationships,[1−4] which have generally focused on linking geometric microstructural characteristics to their bulk mechanical responses. Microstructural features such as pore size, shape, distribution, cell type (e.g., open vs closed), and anisotropies of cellular features are known to have important influences on foam mechanical properties.[1,2] To understand the mechanics of a three-dimensional (3D) cellular solid (or synonymously, "foam"), beam theory has been used to analyze the responses of a two-dimensional (2D) "honeycomb" structure to loading, with scaling laws used to extend these analyses to foams with more complicated 3D geometries. Such scaling arguments result in correlations between the macroscopic mechanical properties of a foam and its relative density, $\rho^* = \rho_f/\rho_s$, where ρ_f is the density of the foam and ρ_s is the density of the nonporous framework material alone. Bulk mechanical parameters of interest include the Young's modulus of the foam, E_f, and the intrinsic Young's modulus of the framework material, E_s. Although these scaling correlations provide estimates of important bulk mechanical properties, correlations to cell microstructures are often uncertain, in part because the 3D pore structures are often heterogeneous and characterized by broad distributions of dimensions that are difficult to analyze quantitatively. In addition, macroscopic mechanical parameters include not only microstructural but also molecular contributions.

For elastomeric polymers, of which the framework materials of common foams are comprised, macroscopic mechanical properties are often dictated by polymer network structures and local compositions. For example, polymer network structures, such as the degree, distribution, and type of cross-linking sites, the molecular weights of cross-linking chains, the density of polymer network entanglements, and elastically ineffective

Received: March 12, 2015
Revised: July 2, 2015
Published: July 15, 2015

DOI: 10.1021/acs.macromol.5b00532
Macromolecules 2015, 48, 4835−4849

Scheme 1. Reactants and Organosiloxane Polymer Products from Network Cross-Linking (PDMS + PMHS) and Organic Functionalization (DPMS + PMHS) Reactions During Syntheses of Hydrogen-Blown Organosiloxane Foams

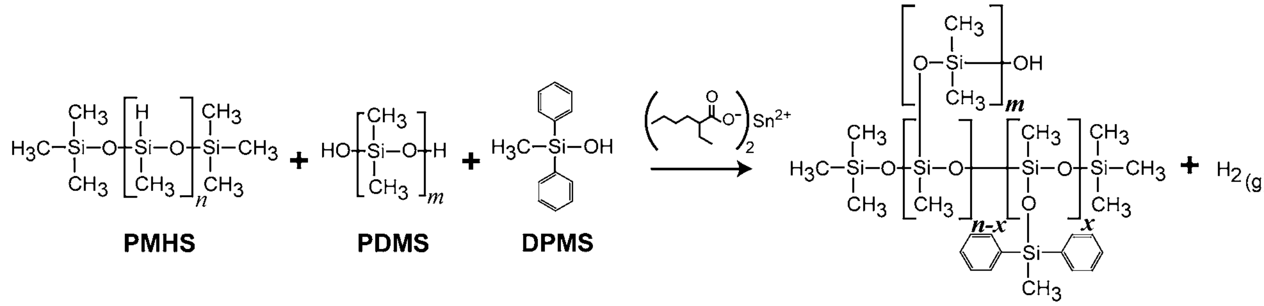

chains (e.g., dangling end chains, loops, un-cross-linked species, etc.), are known to affect the bulk mechanical properties of macromolecular materials, including foams.[5,6] In addition, elastomers may be synthesized with diverse compositions and architectures, such as in polymer−polymer blends,[7,8] block copolymers,[9] or polymers with modified side-chain groups (e.g., organosiloxanes with phenyl side-chain moieties),[10] all of which exhibit different mechanical responses. Elastomeric polymers are also commonly reinforced by the addition of inorganic filler particles, such as silica or clay particulates[11] or ceramic nanoparticles,[12] which result in stiffer materials. Thus, both the network structures and local compositions of elastomers, including elastomeric foams, are expected to play crucial roles in their bulk mechanical properties.

To understand the origins of the mechanical properties of materials that are both elastomeric and cellular, it is therefore important to distinguish and quantify the relative contributions of specific molecular and microstructural characteristics to their macroscopic mechanical responses. Here, the local compositions, molecular structures and interactions, polymer chain dynamics, and pore microstructures of elastomeric organosiloxane foams are collectively and quantitatively measured and correlated with their bulk mechanical properties. The organosiloxane foams are synthesized from blends of the reactive siloxane polymer methyl-terminated polymethylhydrosiloxane (PMHS), a cross-linking siloxane polymer hydroxyl-terminated polydimethylsiloxane (PDMS), and an aromatic species diphenylmethylsilanol (DPMS), with inorganic diatomaceous-earth filler particles in selected samples (Scheme 1). Hydrogen-blown open-cell organosiloxane foams with spherical pore structures were synthesized within a narrow relative density range ($\rho^* = 0.22 \pm 0.01$, or ±5% relative uncertainty), but with systematic compositional differences, including different extents of polymer cross-linking, concentrations of DPMS species, mass fractions of low- to high-molecular-weight PDMS cross-linking chains, and diatomaceous-earth filler contents. The foams exhibited significant differences in their bulk mechanical responses, as measured by uniaxial compression tests. Quantitative micro-X-ray computed tomography (MXCT) analyses establish that micron-scale pore features, such as average cell sizes and size distributions, are similar and cannot account for the large differences in the bulk mechanical properties. In contrast, solid-state nuclear magnetic resonance (NMR) measurements reveal significant differences in local compositions, network structures, and polymer chain dynamics within the elastomeric frameworks that correlate with and account for the different mechanical responses. The mechanical properties of the organosiloxane foams are shown to be controllable by adjusting the molecular compositions and properties of the framework material, independent of cell microstructures.

EXPERIMENTAL METHODS

Material Design, Syntheses, and Compositions. Elastomeric organosiloxane foams were synthesized with methyl-terminated PMHS (NuSil) as a reactive siloxane backbone, hydroxyl-terminated high- and low-molecular-weight PDMS (NuSil) as a cross-linking polymer, and DPMS (NuSil) as an organic side-chain functionality. During synthesis, PMHS silane (Si−H) groups react with PDMS or DPMS silanol (Si−OH) groups, forming Si−O−Si bonds and liberating H_2 gas *in situ* (Scheme 1), which imparts porosity to the foam. As the cross-linking reactions between PDMS and PMHS proceed, the framework develops mechanical stability, while the reactions between DPMS and PMHS increase the concentration of phenyl side-chain moieties bonded to the siloxane backbones. The reactions are catalyzed at room temperature with stannous-2-ethylhexanoate (Sigma-Aldrich). PDMS and PMHS precursor species were characterized by solution-state single-pulse ^1H NMR to determine the number-average molecular weight (M_n) and number of reactive silanol or silane functional groups (f) for each precursor species: for high- and low-molecular-weight PDMS, $f = 2$ and $M_n = 29\,200$ and 730 g/mol, respectively; for PMHS, $f = 50$ and $M_n = 3200$ g/mol. Diatomaceous-earth filler particles (Celite) with hydroxylated silica surfaces (average particle size of 8 μm, BET surface area of 9 m^2/g) were added to selected samples. Differing extents of organosiloxane cross-linking, concentrations of DPMS side-chain groups, and diatomaceous-earth filler contents are expected to influence the bulk mechanical properties of the foams.

The organosiloxane foams were synthesized by first preparing liquid resins with the desired compositions of PMHS, PDMS, and DPMS. Stannous-2-ethylhexanoate was added to ca. 20 g of resin in a Teflon shot injector, such that the final catalyst content was 5 mass %. The mixture was then sheared at 1000 rpm for 10 s and injected into a cylindrical stainless steel mold with a 152 mm (6 in.) inner diameter and 6 mm (1/4 in.) metal spacers. The mold was bolted shut for 15 min to allow network cross-linking and functionalization reactions (Scheme 1) to proceed at autogenous pressure. Jack screws were used to open the mold and release pressure built up from *in situ* H_2 evolution. After 24 h at room temperature, the foams were postcured at 120 °C for 3 h to remove low-molecular-weight components and to ensure completion of cross-linking and functionalization reactions. To determine the postcure densities of the foams, each sample was weighed and its bulk dimensions were measured with a linear variable differential transformer (LVDT) at multiple locations and averaged to obtain representative values.

Organosiloxane resin compositions were selected such that the foams exhibited significant differences in molecular compositions but similar cell microstructures. This result was achieved by following a design principle whereby the fraction of total silanol/silane functional groups, ϕ, was held constant across the different resin compositions. Doing so fixed the stoichiometric amount of H_2 gas generated *in situ* within the mold because the siloxane backbone reactions usually proceed to completion. The fraction of silanol/silane functional groups

ϕ may be determined from the initial synthesis compositions according to

$$\phi = \frac{X_{\mathrm{PDMS,H}}(\hat{f}_{\mathrm{PDMS,H}}) + X_{\mathrm{PDMS,L}}(\hat{f}_{\mathrm{PDMS,L}}) + X_{\mathrm{DPMS}}(\hat{f}_{\mathrm{DPMS}})}{X_{\mathrm{PMHS}}(\hat{f}_{\mathrm{PMHS}})} \qquad (1)$$

where $\hat{f}_i \equiv f_i/M_{\mathrm{n},i}$ are the moles of silanol or silane functional groups per unit mass, X_i is the mass fraction of species i, and the subscripts PDMS,H and PDMS,L represent high- and low-molecular-weight PDMS, respectively. Since ϕ was constant for each foam composition, it was convenient to fix the total number of silane groups by using identical mass fractions of PMHS, while varying the total number of silanol groups by using differing PDMS and DPMS contents. Arbitrarily, the mass fraction of PMHS in the different organosiloxane foam resins was fixed at $X_{\mathrm{PMHS}} = 0.06$. The PDMS and DPMS contents were then systematically varied among the different resin compositions to alter the relative extents of cross-linking and concentrations of DPMS side-chain groups. The DPMS content for each organosiloxane foam composition was then selected, and the corresponding mass fractions of high- and low-molecular-weight PDMS were computed using eq 1 and the overall mass balance, $X_{\mathrm{PDMS,H}} + X_{\mathrm{PDMS,L}} + X_{\mathrm{PMHS}} + X_{\mathrm{DPMS}} + X_{\mathrm{diat}} = 1$, where the subscript diat represents the diatomaceous-earth filler. When added, the mass fraction of diatomaceous-earth filler was arbitrarily fixed at $X_{\mathrm{diat}} = 0.15$.

To synthesize a foam with relatively uniform macroscopic density, three interrelated time scales must be appropriately balanced *in situ*: (i) PMHS−PDMS cross-linking kinetics must proceed at a rate sufficient to impart structural stability, while (ii) H_2 gas evolution occurs at a rate sufficient to impart micron-scale porosity, before (iii) the resin itself drains to the bottom of the mold. Experimentally, silanol/silane fractions of $\phi = 0.75$ produced a range of resin formulations that were feasibly synthesized according to these time scales. Five different resin compositions were examined to determine the effects of varying network cross-linking densities and organic functionalities on the bulk mechanical properties of the resulting foams. These compositions are summarized in Table 1 and are reported for three foams with differing DPMS contents: $X_{\mathrm{DPMS}} = 0.02$ (foam I), 0.05 (II), and 0.08 (III), which are expected to produce decreasing extents of cross-linking. In addition, to evaluate the effects of varying the silanol/silane fractions ϕ or the incorporation of filler particles, two additional foams were synthesized with $X_{\mathrm{DPMS}} = 0.05$ and either a lower silanol/silane fraction $\phi = 0.50$ (IV) or with diatomaceous-earth filler particles (V).

Table 1. Synthesis Compositions of the Five Organosiloxane Foams Examined in This Work[a]

foams	I	II	III	IV	V
X_{DPMS}	0.02	0.05	0.08	0.05	0.05
$X_{\mathrm{PDMS,H}}$	0.71	0.73	0.76	0.82	0.58
$X_{\mathrm{PDMS,L}}$	0.21	0.16	0.10	0.07	0.16
X_{PMHS}	0.06	0.06	0.06	0.06	0.06
X_{diat}					0.15
ϕ	0.75	0.75	0.75	0.50	0.75

[a] Notation: X_i, mass fraction of species i; ϕ, fraction of silanol/silane functional groups determined using eq 1.

To compare accurately the stress−strain properties of foams prepared with different resin formulations, all samples were synthesized within a narrow range of postcure relative densities, ρ^*. The postcure densities of the foams, ρ_f, depended upon the initial weight of the resin, the volume of the mold, the weight of released volatiles (e.g., low-molecular-weight silicone species), and bulk volume shrinkages (small but non-negligible) that occur during the postcuring process. The densities of the framework material, ρ_s, were assumed to be identical to the densities of the resin mixtures, which were $\rho_s = 0.99$ and 1.08 g/cm^3 for resins without and with diatomaceous-earth filler particles, respectively. The relative densities of all samples were $\rho^* = 0.22 \pm 0.01$, where the uncertainties were determined from propagation-of-error analyses.

Micro-X-ray Computed Tomography. MXCT measurements[13−15] were acquired using an Xradia MXCT system. 3D tomographic data sets were collected on cylindrical samples (6 mm diameter and height) using a Hamamatsu Photonics 5 μm microfocus tungsten X-ray source that operated at 80 kV acceleration voltage and 4 W of power, which directed a beam of X-rays in a 43° cone through each sample. The samples were mounted on a microvacuum tip on a four axis (x, y, z, θ) stage. The X-rays passed through the sample and excited a scintillator material mounted on the front of a normal microscope objective, converting the X-ray photons to visible light, which was imaged with a 2k × 2k piezoelectrically cooled charged-coupled device (CCD). A 4× magnification objective with a field of view of 6.2 mm produced images on the CCD with a pixel size of 3.025 μm. The sample was radiographed with 1 min exposures, rotated slightly, and re-exposed; the process continued until 1000 images were collected over 180°. The total exposure time was approximately 18 h per foam sample. The radiographs were reconstructed by binning the data by a factor of 2 to produce a series of 2D MXCT images with a size of pixel 6.050 μm. The voxel size between 2D slices was 10 μm. Pore sizes and distributions were quantitatively analyzed using a custom image analysis program specifically designed to identify structural features from a series of 2D MXCT images (see Supporting Information for more details).

Uniaxial Compression Testing. Uniaxial compression tests were conducted at room temperature on cylindrical foam samples (152 mm diameter, 6 mm height) between circular 152 mm diameter parallel plates on an MTS Insight 30 load frame with a calibrated 2.5 kN load cell. A sample was placed between the plates and preloaded to 4.5 N; this position was defined as the "zero height" reference position. Each sample was compressed at 1.3 mm/min to 65% strain and unloaded at 1.3 mm/min to its original height. The foams experienced a strain-induced softening upon mechanical compression, reaching a consistent response after the fourth compression cycle. The stress−strain curves reported for each foam composition are the average responses of four distinct samples synthesized from the same resin mixture.

Nuclear Magnetic Resonance Spectroscopy. Solid-state ^{1}H and ^{29}Si NMR measurements were performed on a Bruker AVANCE IPSO 500 NMR spectrometer with an 11.74 T wide-bore superconducting magnet operating at 500.13 and 99.35 MHz for ^{1}H and ^{29}Si nuclei, respectively. Bruker ^{1}H/X double-resonance magic-angle-spinning (MAS) probeheads with 4 or 1.3 mm diameter zirconia rotors were used, with samples rotated at 6 to 10 kHz or 60 kHz, respectively. Low-temperature NMR experiments were conducted by pumping cooled N_2 gas through the probehead under temperature regulation. All ^{1}H and ^{29}Si NMR measurements were conducted using radio frequency (rf) field strengths of 73.5 kHz ($\pi/2$ pulse of 3.4 μs) and 59.5 kHz ($\pi/2$ pulse of 4.2 μs), respectively. All ^{29}Si NMR spectra were acquired with proton decoupling using the SPINAL-64 pulse scheme[16] with a ^{1}H rf field strength of 67.5 kHz. ^{1}H and ^{29}Si chemical shifts were referenced to tetramethylsilane (TMS, $Si(CH_3)_4$) with tetrakis(trimethylsilyl)silane (TKS, $Si[Si(CH_3)_3]_4$) as a secondary chemical shift reference.

Single-pulse ^{1}H and ^{29}Si experiments were calibrated with respect to the longitudinal relaxation times (T_1) of the different moieties to ensure fully quantitative spectra, with recycle delays of 2.5 and 10 s for ^{1}H and ^{29}Si nuclei, respectively. ^{29}Si{^{1}H} cross-polarization (CP)-MAS measurements were conducted with adiabatic passage through the Hartmann−Hahn condition[17] using a contact time of 4 ms. The 2D ^{29}Si{^{1}H} HETCOR NMR experiment[18,19] is a 2D extension of the 1D ^{29}Si{^{1}H} CP-MAS NMR measurement, enabling the chemical shifts of dipole−dipole-coupled ^{29}Si and ^{1}H moieties to be resolved in two frequency dimensions. Longitudinal ^{1}H magnetization was rotated to the transverse plane with a 90° rf pulse and then allowed to evolve for an incremented spin-evolution time t_1 prior to transfer of magnetization from ^{1}H to ^{29}Si nuclei by cross-polarization (4 ms). The subsequent ^{29}Si free-induction decays were measured directly during the detection period t_2. Double Fourier transformation converted the time domain signals $S(t_1,t_2)$ into frequencies $F(\omega_1,\omega_2)$ that are presented as 2D contour plot spectra (contours presented to 5% of full signal intensity). States quadrature detection[20] was used in the indirect dimension.

Transverse ^{1}H relaxation time (T_2) measurements were conducted at room temperature under static conditions with the Hahn spin−echo pulse sequence.[19] The attenuation of transverse ^{1}H magnetization were fit to triexponential curves by linear regression according to

$$\frac{I(\tau)}{I_0} = X_N e^{\tau/T_{2,N}} + X_D e^{\tau/T_{2,D}} + X_U e^{\tau/T_{2,U}} \qquad (2)$$

where I is the integrated ^{1}H signal intensity, I_0 is the signal intensity when no echo delay is used, τ is the full-echo delay time, and X_i are the relative populations of ^{1}H nuclei that exhibit transverse ^{1}H relaxation times $T_{2,i}$. The ^{1}H signal intensities of the siloxane methyl protons at 0.1 ppm were measured while full-echo delays τ were incremented by 50 μs from 0 to 60 ms. The subscripts N, D, and U indicate ^{1}H siloxane moieties associated with network chains, dangling end chains, and un-cross-linked species, respectively. To fit the transverse ^{1}H relaxation data, the NMR signal attenuations were first fit to a single exponential between τ = 40 and 60 ms to determine X_U and $T_{2,U}$ because at these echo delays the un-cross-linked species predominantly contribute to the net transverse ^{1}H magnetization. The data were then fit to a biexponential between τ = 15 and 60 ms to determine X_D and $T_{2,D}$ since at these echo delays only the dangling end chains and un-cross-linked species contribute to the NMR signals. X_N was then computed by molar balance according to $X_N = 1 - X_D - X_U$, and subsequently the entire transverse ^{1}H relaxation data were fit according to eq 2 to determine $T_{2,N}$.

■ RESULTS AND DISCUSSION

Cell Microstructures. MXCT and image processing techniques were used to quantify and compare the pore sizes and distributions of the organosiloxane foams. For example, processed MXCT images of a representative foam are shown in Figure 1. A cylindrical sample was analyzed with MXCT, generating a series of 2D image slices orthogonal to the axial (z) direction that have been reconstructed into a 3D image (Figure 1a, inset). To facilitate 3D image processing, a cuboidal subset of this cylindrical geometry was chosen as the volume of interest for quantitative image processing (Figure 1a). Using a series of 2D MXCT images orthogonal to the z-axis of the foam sample, a series of 2D images were subsequently reconstructed orthogonal to the x-axis. Representative 2D MXCT slices orthogonal to both the z- and x-axes of the foam are shown in Figures 1b and 1c, respectively, where red curves represent circular fits of each pore.

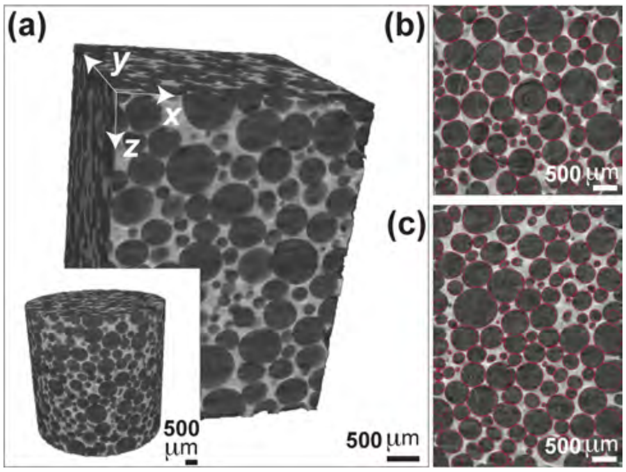

Figure 1. MXCT images of a cylindrical organosiloxane foam with X_{DPMS} = 0.05 and a silanol/silane fraction ϕ = 0.75 (foam II). (a) Reconstructed 3D image of the volume of interest. The lighter areas are the organosiloxane framework, and the darker areas are pores. Inset: 3D image of the macroscopic sample. Representative 2D MXCT images are shown orthogonal to the (b) z- and (c) x-axes. Red curves represent circular fits to each pore.

Subsequent image processing permits quantitative analyses of the 2D and 3D microstructural features of the different organosiloxane foams. For example, the mean 2D pore radii R per MXCT image orthogonal to the z- (R_z) and x-axes (R_x) are plotted in Figure S1 (Supporting Information), respectively, as functions of depth along their respective axes. Both R_z and R_x fluctuate around the bulk-averaged 2D pore radii $\overline{R}_z$ and $\overline{R}_x$ with standard deviations $\sigma_{R,z}$ and $\sigma_{R,x}$, respectively, which are reported in Table 2 for the different organosiloxane foams.

Table 2. Microstructural Properties of Elastomeric Organosiloxane Foams Synthesized with the Compositions in Table 1[a]

foams	I	II	III	IV	V
2D pore analyses					
$\overline{R}_z$ (μm)	154	157	195	160	205
$\sigma_{R,z}$ (μm)	15	11	15	15	15
$\overline{R}_x$ (μm)	149	154	152	152	216
$\sigma_{R,x}$ (μm)	6	6	10	8	19
3D pore analyses					
$\overline{P}_z$ (μm)	134	136	175[b]	142	154
$\sigma_{P,z}$ (μm)	80	87	104[b]	86	121
$\overline{P}_x$ (μm)	133	131	177[b]	137	165
$\sigma_{P,x}$ (μm)	80	85	109[b]	81	130

[a] Notation: $\overline{R}_i$, bulk-averaged 2D pore radii with standard deviation $\sigma_{R,i}$; $\overline{P}_i$, bulk-averaged 3D pore radii with standard deviation $\sigma_{P,i}$; subscripts z and x indicate MXCT analyses orthogonal to z- and x-axes, respectively. [b] Estimated spherical pore shape.

Because the porosities of these self-blown foams are generated *in situ*, the fluctuations in 2D pore sizes along the z- and x-axes may be the result of local differences in H_2 bubble nucleation and growth that arise due to inhomogeneities in the distributions of reacting species (e.g., DPMS, tin catalyst, etc.).

The probability density functions of 3D pore radii were also computed, enabling further microstructural comparisons between the different organosiloxane foams. The 2D analyses do not permit the accurate computation of such probability density functions, as any 3D pore with a radius that is greater than the spacing between 2D images (10 μm) will be counted multiple times in adjacent frames. Both the z- and x-axis series of consecutive 2D images were analyzed separately to compute the locations, sizes, and total number of 3D pores, yielding two distinct estimates of 3D pore radii P_z and P_x, respectively. The probability density functions of 3D pore radii PDF$_z$ and PDF$_x$ are shown in Figures 2a and 2b, respectively, which indicate the distributions of 3D pore radii analyzed with respect to the z- (P_z) and x-axes (P_x). The bulk-averaged 3D pore radii $\overline{P}_z$ and $\overline{P}_x$ and their standard deviations $\sigma_{P,z}$ and $\sigma_{P,x}$ (which reflect the widths of the distributions of 3D pore sizes) are reported in Table 2. The experimentally determined probability density functions were compared with theoretical distributions obtained using the method of maximum-likelihood estimates. Common probability distributions (e.g., log-normal, Weibull)

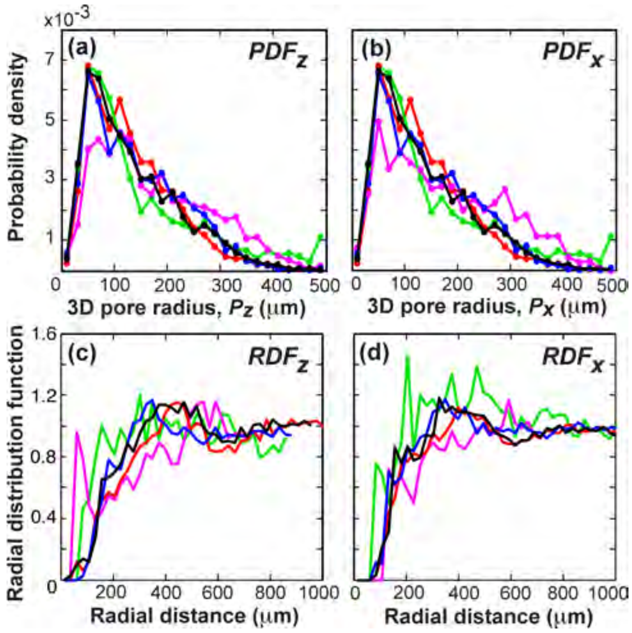

Figure 2. Probability density functions of 3D pore radii (a) PDF_z and (b) PDF_x and radial distribution functions of 3D pore locations (c) RDF_z and (d) RDF_x, which were computed from the sizes and locations of 3D pores analyzed with respect to the z-and x-axes, respectively. Data are shown for foams I (blue), II (black), III (magenta), IV (red), and V (green).

and multiple overlapping distributions (e.g., two normal distributions) do not fit the 3D pore size data within a 90% confidence interval, according to Pearson's χ^2 goodness-of-fit test.[21] Thus, simple distributions do not adequately fit the experimental probability density functions, reflecting that pore formation is a complicated function of many factors, such as local compositions, reaction kinetics, and rheology.

Comparisons of the radial distribution functions of 3D pore locations yield additional insights into the local cell microstructures of the different organosiloxane foams. The radial distribution functions reflect the average number density of 3D pores as a function of the radial distance from a given pore, normalized by the bulk number density of 3D pores. The radial distribution functions of 3D pore locations RDF_z and RDF_x are shown in Figures 2c and 2d, respectively, which were computed from the locations of 3D pores analyzed with respect to the z- and x-axes. The curves establish that the organosiloxane foams exhibit highly disordered pore structures, as indicated by the absence of strong local maxima and minima above the noise level, particularly far away (e.g., several average 3D pore radii) from a given pore.

The quantitative MXCT analyses collectively establish that the organosiloxane foams, despite having large differences in their molecular compositions, exhibit similar cell microstructures. In particular, foams I, II, and IV have very similar microstructures, while foam III (with the highest DPMS content) and foam V (with diatomaceous-earth filler) have modestly larger pore dimensions, though otherwise share similar microstructural characteristics compared to the other foams (see Supporting Information for more details). For all of the foams examined, the bulk-averaged 2D pore radii fall within the ranges of $\overline{R}_z$ = 154–205 μm and $\overline{R}_x$ = 149–216 μm when analyzed orthogonal to the z- and x-axes, respectively, with corresponding standard deviations in the ranges of $\sigma_{R,z}$ = 11–15 μm and $\sigma_{R,x}$ = 6–19 μm. In addition, the probability distribution functions of 3D pore radii are similar for the different organosiloxane foams when analyzed orthogonal to both the z- and x-axes (Figure 2a,b). The bulk-averaged 3D pore radii fall within the ranges of $\overline{P}_z$ = 134–175 μm and $\overline{P}_x$ = 133–177 μm, with corresponding standard deviations of the size distributions of $\sigma_{P,z}$ = 80–121 μm and $\sigma_{P,x}$ = 80–130 μm, respectively. The radial distribution functions of 3D pore locations are also similar when analyzed orthogonal to both the z- and x-axes (Figure 2c,d). Compared to foams I, II, and IV, these functions for foams III and IV exhibit higher noise levels due to their larger standard deviations of 3D pore radii ($\sigma_{P,z}$ and $\sigma_{P,x}$). The different organosiloxane foams thus have similar microstructural features that cannot account for their significantly different mechanical properties, as shown below.

Bulk Mechanical Properties. Despite similarities in their cell microstructures, the organosiloxane foams exhibit significantly different macroscopic mechanical properties that are correlated with the compositions and network characteristics of their frameworks. These differences are established by uniaxial compression tests (Figure 3), where the stress σ is plotted as a

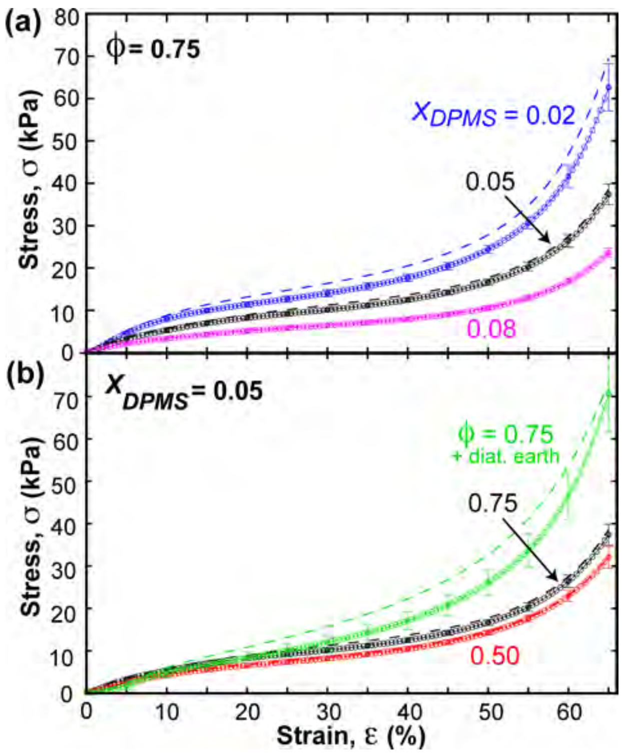

Figure 3. Plots of stress σ as functions of strain ε measured for the different organosiloxane foams under compressive loading at room temperature. (a) Foams synthesized with identical silanol/silane fractions ϕ = 0.75, but with different DPMS contents: X_{DPMS} = 0.02 (blue), 0.05 (black), and 0.08 (magenta), corresponding to foams I, II, and III, respectively. (b) Foams synthesized with identical DPMS contents (X_{DPMS} = 0.05), but with different silanol/silane fractions (ϕ) and/or filler contents: ϕ = 0.75 (black), (b) ϕ = 0.50 (red), and (c) ϕ = 0.75 with diatomaceous-earth filler (X_{diat} = 0.15, green), corresponding to foams II, IV, and V, respectively. Measurements were made over a series of loading/unloading cycles, with results shown for the first (dashed curves) and fourth (solid curves) loading cycles. Each mechanical response is the average of four samples, and uncertainty bars (shown at regular intervals) represent one standard deviation about the mean. For clarity, unloading cycles are not shown.

DOI: 10.1021/acs.macromol.5b00532
Macromolecules 2015, 48, 4835–4849

Table 3. Mechanical Properties of Elastomeric Organosiloxane Foams Synthesized with the Compositions in Table 1[a]

foams	I	II	III	IV	V
E_f (kPa)	1.00 ± 0.04	0.66 ± 0.05	0.40 ± 0.04	0.50 ± 0.03	0.58 ± 0.06[b]
E_s (kPa)	20.9 ± 0.8	14.0 ± 0.8	8.3 ± 1.0	10.3 ± 0.6	12.0 ± 1.4
$\sigma_{50\%}$ (kPa)	24.5 ± 0.9	16.7 ± 0.7	10.6 ± 0.6	14.3 ± 0.6	26.0 ± 3.0

[a] Notation: E_f, Young's moduli of foam; E_s, Young's moduli of (nonporous) framework material determined using eq 3; $\sigma_{50\%}$, stress at 50% strain. [b] Fit within 5−10% strain.

function of strain ε during compressive loading. Figure 3a depicts the stress−strain behaviors of foams synthesized with identical fractions of silanol/silane functional groups (ϕ = 0.75), but with differing DPMS contents and resulting extents of cross-linking (foams I, II, and III). The loading cycles of these organosiloxane foams resemble those of low-density foams with strutlike morphologies and exhibit three qualitatively different stress−strain regimes.[1] At small strains ($\varepsilon \lesssim$ 0−5%), linear stress−strain behavior is observed, known as "strut bending", where cell frameworks (struts) within the microstructure bend elastically. At intermediate strains ($\varepsilon \approx$ 5−60%), the material exhibits nonlinear "strut buckling" behavior, where struts fail under applied stress and pore structures begin to collapse. This nonlinear regime is responsible for the energy absorption capabilities of the foams, where the energy absorbed per unit volume corresponds to the area under the stress−strain curve. At large strains ($\varepsilon \gtrsim$ 60%), "densification" occurs, whereby the struts fail, porosity decreases significantly, and the bulk framework material is compressed. For these organosiloxane foams, the first loading cycle (dashed curves) requires more stress to achieve a given level of strain than the second cycle; the mechanical responses trace reproducible paths after the fourth load cycle (solid curves). Unloading cycles (not shown for clarity) exhibit hysteresis behaviors that are characteristic of elastomeric polymers, responses that are attributed to the viscoelastic behaviors of mobile portions of the network.[22]

The stress−strain curves enable quantitative comparisons of the mechanical properties among the different organosiloxane foams. The elastic stiffness at small strains is measured by the Young's modulus of the foams, E_s, which corresponds to the rate of change of stress σ with respect to strain ε in the linear regime. The Young's modulus of the (nonporous) framework, E_s, is also useful for correlating differences in the compositions of the polymer networks with the mechanical responses of the foams. Whereas E_f may be determined from the slope of the linear stress−strain regions, E_s must be estimated because synthesizing a nonporous organosiloxane material is difficult due to *in situ* evolution of H_2 gas. Here, E_s values have been estimated by using a well-established structure−property scaling model[3] for 3D cellular solids

$$\frac{E_f}{E_s} = c\left(\frac{\rho_f}{\rho_s}\right)^2 \tag{3}$$

where c is an experimentally determined constant of proportionality. Experimental data[1] on open-cell foams with varying relative densities indicate that $c \approx 1$ for a wide range of diverse cellular materials (e.g., elastomers, rigid polymers, and glasses). It is also informative to compare mechanical behaviors in the nonlinear stress−strain regime, where a stiffer material requires a greater stress to achieve a given strain. Here, the stress at 50% strain, $\sigma_{50\%}$, has been arbitrarily chosen to compare the mechanical responses of the organosiloxane foams at higher strains. Values for E_f, E_s, and $\sigma_{50\%}$ are reported in Table 3 for each of the different foam compositions listed in Table 1.

Organosiloxane foams synthesized with identical silanol/silane fractions ϕ, but different DPMS contents and extents of cross-linking, exhibit significantly different mechanical behaviors. The stress−strain curves shown in Figure 3a are the mechanical responses of foams synthesized with ϕ = 0.75, but with X_{DPMS} = 0.02 (foam I), 0.05 (II), or 0.08 (III), which exhibit Young's moduli of E_f = 1.00 ± 0.04, 0.66 ± 0.05, and 0.40 ± 0.04 kPa and E_s = 20.9 ± 0.8, 14.0 ± 0.8, and 8.3 ± 1.0 kPa, respectively. Therefore, lower concentrations of DPMS side-chain groups and correspondingly larger numbers of PDMS cross-linking sites result in stiffer materials (e.g., foams I and II) at small strains. Similarly, such foams are also stiffer at larger strains, with $\sigma_{50\%}$ = 24.5 ± 0.9 and 16.7 ± 0.7 kPa for foams I and II, respectively, compared to 10.6 ± 0.6 kPa for foam III. Thus, organosiloxane foams with lower DPMS concentrations and higher extents of cross-linking are stiffer at both small and large strains.

Organosiloxane foams synthesized with lower silanol/silane fractions ϕ or higher diatomaceous-earth filler contents also yield materials with significantly different mechanical responses. The stress−strain curves shown in Figure 3b correspond to foams synthesized with identical DPMS contents of X_{DPMS} = 0.05, but with ϕ = 0.75 (foam II), with ϕ = 0.50 (foam IV), or with ϕ = 0.75 and including diatomaceous-earth filler X_{diat} = 0.15 (foam V). Comparing the materials with different silanol/silane fractions, foam II with ϕ = 0.75 exhibits larger Young's moduli, with E_f = 0.66 ± 0.05 kPa and E_s = 14.0 ± 0.8 kPa, compared to foam IV with ϕ = 0.50, for which E_f = 0.50 ± 0.03 kPa and E_s = 10.3 ± 0.6 kPa. Similar trends are observed at larger strains, with $\sigma_{50\%}$ = 16.7 ± 0.7 kPa for ϕ = 0.75 (II), compared to $\sigma_{50\%}$ = 14.3 ± 0.6 kPa for ϕ = 0.50 (IV). Thus, for this class of organosiloxane foams, the materials synthesized with lower silanol/silane fractions ϕ are moderately softer at both small and large strains. Analyzing the effect of filler content, foam V with X_{diat} = 0.15 exhibits smaller Young's moduli of E_f = 0.58 ± 0.06 kPa and E_s = 12.0 ± 1.4 kPa, compared to similar values of E_f = 0.66 ± 0.05 kPa and E_s = 14.0 ± 0.8 kPa for foam II without filler. However, for foam V with the filler particles, linear responses are only observed at higher strains, $\varepsilon \approx$ 5−10%, as opposed to $\varepsilon \approx$ 0−5% for the organosiloxane foams without filler. Thus, the addition of filler particles alters the linear stress−strain behavior but does not otherwise result in significant changes of the effective Young's moduli. For larger strains, the applied stress necessary to achieve a given strain continues to increase significantly, relative to foams without filler, with $\sigma_{50\%}$ = 26.0 ± 3.0 and 16.7 ± 0.7 kPa measured for foam V with and for foam II without filler, respectively. Thus, organosiloxane foams synthesized with lower silanol/silane fractions ϕ are moderately softer at all strains, while foams synthesized with diatomaceous-earth filler particles are substantially stiffer at large strains, though their

DOI: 10.1021/acs.macromol.5b00532
Macromolecules 2015, 48, 4835−4849

mechanical properties are not significantly affected at small deformations.

Further analyses of the stress−strain curves in Figure 3 reveal insights into possible origins of the strain-induced softening, known as the Mullins effect,[23] which is observed between the first and fourth compression loading cycles. As noted in a review by Diani et al.,[24] the molecular origins of the Mullins effect are still a matter of debate. In addition, few studies of the Mullins effect have been conducted on unfilled elastomers.[25−28] For the unfilled organosiloxane foams in this work (foams I−IV), the magnitude of the Mullins effect depends on the relative mass fractions of low- (short) to high-molecular-weight (long) cross-linking PDMS chains ($X_{\mathrm{PDMS,L}}/X_{\mathrm{PDMS,H}}$), which may be estimated from Table 1. For example, in Figure 3a, the foams synthesized with X_{DPMS} = 0.02 and with a relatively high fraction (0.30) of low- to high-molecular-weight PDMS exhibit a significant Mullins effect, as manifested by the lower stresses at a given strain during the fourth loading cycle, compared to the first, across the entire range of strain investigated. By comparison, foams prepared with X_{DPMS} = 0.08 and a correspondingly low fraction (0.13) of low- to high-molecular-weight PDMS exhibit no Mullins effect within the sensitivity limits of the measurement. Comparing the foams without diatomaceous-earth filler in Figure 3b, the foams synthesized with ϕ = 0.75 and with a moderate fraction (0.22) of low- to high-molecular-weight PDMS exhibit a small but finite Mullins effect. In contrast, the foams prepared with ϕ = 0.50 and with a low fraction (0.09) of low- to high-molecular-weight PDMS exhibit no observable Mullins effect. Thus, decreasing the fraction of low- (short) to high-molecular-weight (long) cross-linking PDMS chains correlates with a significant decrease (and even elimination) of the strain-induced softening. Among the competing hypotheses that have been proposed to explain the Mullins effect,[11,24] these results appear to be consistent with the work of Harwood et al.,[27] who suggest for unfilled networks that strain softening in elastomeric polymers is due to quasi-irreversible network deformations associated with short polymer chains that are completely extended. Lastly, the organosiloxane foams with diatomaceous-earth filler particles show the largest strain-induced softening, as evidenced in Figure 3b by the significantly smaller stresses measured at a given strain after several loading/unloading cycles. This result is consistent with observations that filled elastomers exhibit a greater Mullins effect, compared to unfilled elastomers, and may be due to the breakage of filler particle agglomerates or the reorganization of the filler particles during the initial compression cycles.[24,29]

Molecular Compositions, Structures, Interactions, and Polymer Chain Dynamics. While significant differences in the mechanical properties of the organosiloxane foams are not ascribable to their similar cell microstructures, the molecular compositions, structures, interactions, and polymer chain dynamics in the foam frameworks differ appreciably and are correlated with their macroscopic mechanical properties. Such molecular-level properties can be measured and quantitatively compared with solid-state ^{29}Si and ^{1}H NMR measurements, which are sensitive to the local environments, proximities, and relative mobilities of the constituent atoms and the restricted dynamics of polymer chains in the cross-linked networks.

Quantitative Compositions. To identify distinct ^{29}Si framework moieties and compare their relative populations among the different organosiloxane foams, quantitative single-pulse ^{29}Si MAS NMR spectra were acquired for materials synthesized from each of the resin compositions listed in Table 1. Figure 4a depicts schematic structures of the different moieties present within the organosiloxane foams, along with labels of their ^{29}Si and ^{1}H NMR chemical shift assignments in Arabic and Roman numerals, respectively. The single-pulse ^{29}Si MAS spectra of the foams in Figure 4b−d exhibit three distinct groups of well-resolved signals that are assignable to their various siloxane moieties:[30] "monofunctional" *M* ^{29}Si sites (four-coordinate ^{29}Si atoms, bonded to three carbon atoms and to another Si atom through a bridging oxygen atom) from −11 to −12 ppm, "difunctional" *D* ^{29}Si sites (bonded to two carbon atoms and two other Si atoms each through a bridging oxygen atom) from −19 to −23 ppm, and "trifunctional" *T* ^{29}Si sites

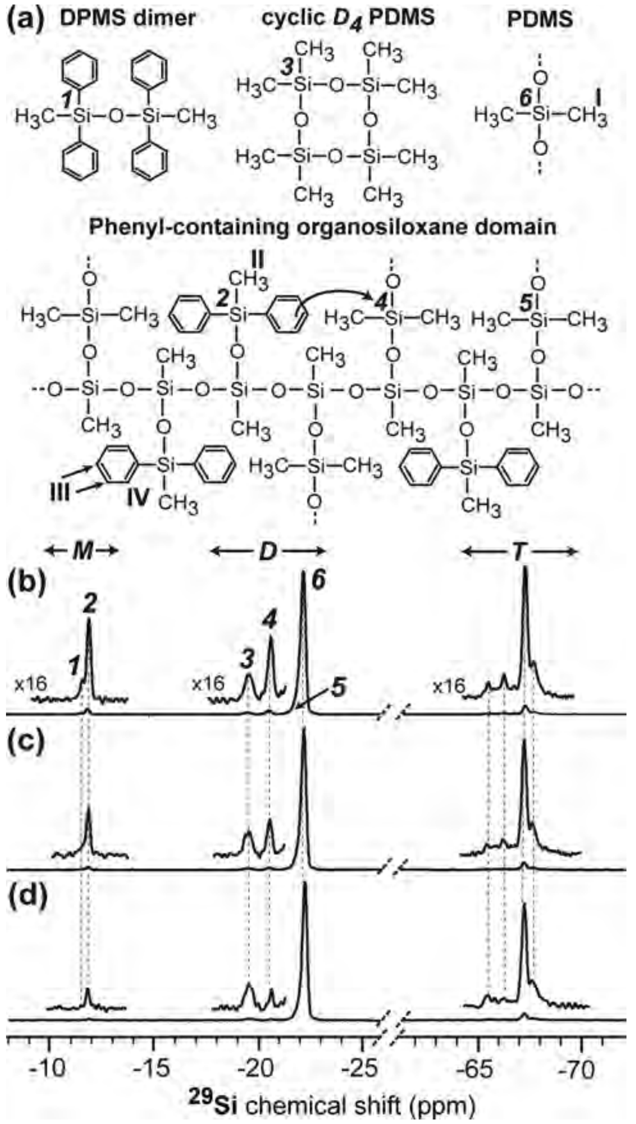

Figure 4. (a) Schematic structures of the different molecular moieties in the organosiloxane foams. (b−d) Solid-state single-pulse ^{29}Si MAS NMR spectra of organosiloxane foams synthesized with identical silanol/silane fractions of ϕ = 0.75, but with different DPMS contents: X_{DPMS} = (b) 0.08, (c) 0.05, or (d) 0.02, corresponding to foams III, II, and I, respectively. The regions of the spectra corresponding to the *M*, *D*, and *T* ^{29}Si species are labeled. ^{29}Si and ^{1}H chemical shift assignments are labeled in (a) with Arabic and Roman numerals, respectively. All spectra were acquired at 10 kHz MAS under ambient conditions.

(bonded to one carbon atom and three other Si atoms through bridging oxygen atoms) from −65 to −69 ppm. Integrating the resolved signal intensities in the single-pulse ^{29}Si MAS spectra allows the relative populations of specific ^{29}Si moieties to be established quantitatively.

The single-pulse ^{29}Si MAS NMR spectra shown in Figure 4b−d were conducted on the same foams (I, II, and III) for which uniaxial compression measurements are reported in Figure 3a. The spectra exhibit similar ^{29}Si signals, but with significant differences in their integrated intensities that indicate notable compositional and structural differences. In Figure 4b, resolved ^{29}Si signals are present at −11.6, −11.9, −19.5, −20.6, −22.2, −65.4, −66.2, −67.1, and −67.6 ppm. The monofunctional *M* ^{29}Si signals at −11.6 and −11.9 ppm are assigned respectively to ^{29}Si atoms in DPMS dimers and to DPMS moieties that are covalently bonded to the organosiloxane backbone, labeled "1" and "2" in Figure 4a, respectively. The difunctional *D* ^{29}Si signals at −19.5, −20.6, and −22.2 ppm are respectively assigned to cyclic D_4 PDMS oligomeric compounds[30] ("3", present in small concentrations in the PDMS precursor materials), PDMS ^{29}Si atoms ("4") along the phenyl-containing organosiloxane backbone that experience through-space magnetic ring currents (see below) from molecularly proximate (<1 nm) DPMS phenyl moieties, and organosiloxane PDMS ^{29}Si atoms ("6") far (>1 nm) from the phenyl-containing organosiloxane backbone moieties. Note that ^{29}Si signals at approximately −9 ppm from cyclic D_3 PDMS oligomers[30] are not observed, presumably because they are removed by the postcure thermal treatment at 120 °C. An unresolved shoulder at ca. −22.0 ppm likely arises from *D* ^{29}Si PDMS atoms ("5") that experience decreased electronic shielding due to their proximities to phenyl-containing moieties on the organosiloxane backbones. Resolved signals at −65.4, −66.2, −67.1, and −67.6 ppm are associated with trifunctional *T* ^{29}Si moieties that are cross-linked to PDMS chains or covalently bonded to DPMS species, for which unambiguous assignments are not possible. Overall, the resolved and quantifiable *M*, *D*, and relative *D*:*T* ^{29}Si signals reveal detailed information regarding the molecular compositions of the foams that can be correlated with their mechanical properties.

Quantitative analyses of the monofunctional *M* ^{29}Si signals establish the extents of DPMS functionalization and PDMS cross-linking reactions among the different organosiloxane foams. Furthermore, the relative integrated *M* ^{29}Si signal intensities at ca. −12 ppm are quantitatively consistent with the relative DPMS contents of the different foams. For example, for foam III synthesized with $X_{\mathrm{DPMS}} = 0.08$ (Figure 4b), this signal is larger by factors of approximately 8/5 and 4, compared to foams II and I synthesized with $X_{\mathrm{DPMS}} = 0.05$ or 0.02, respectively (Figure 4c,d). No signals are observed at −4.4 ppm in any of the spectra from unreacted ^{29}Si DPMS moieties,[31] which indicates that all DPMS species are either covalently bonded to the siloxane backbone ("2") or are present as DPMS dimers ("1"). Spectral deconvolutions and comparisons made among the different foam compositions reveal that approximately 80% of the overall *M* ^{29}Si signals (Figure 4b−d) are due to DPMS side-chain groups in the phenyl-containing organosiloxane domains, whereas the other 20% is associated with DPMS dimers. Because the numbers of initial DPMS silanol groups and PMHS silane groups are known, overall mass balances establish that approximately 8%, 20%, and 32% of the total PMHS silane sites have reacted with DPMS silanol groups during syntheses of foams I, II, and III, respectively. In addition, no signals at −12.9 ppm associated with $(-\mathrm{O}\mathbf{Si}(\mathrm{CH_3})_2\mathrm{OH})$ *M* ^{29}Si moieties from unreacted PDMS silanol end groups are detected within the sensitivity of the NMR measurements. Consequently, approximately 65%, 50%, and 35% of the total PMHS silane sites are estimated to have reacted with PDMS silanol groups during syntheses of foams I, II, and III, respectively. These results establish quantitatively the greater extents of PDMS cross-linking with decreasing DPMS contents, which correlate well with the macroscopic stiffnesses of the respective foams, as measured by uniaxial compression tests (Figure 3a). Such structural features are furthermore consistent with the larger Young's moduli of polymer networks with increased numbers of cross-linking sites.[5,6]

Analyses of the difunctional *D* ^{29}Si signals offer additional insights into the local environments of the PDMS polymer chains and the molecular architectures of the phenyl-containing organosiloxane domains. The intense and well-resolved ^{29}Si signals in Figure 4b−d associated with PDMS ^{29}Si atoms at −22.2 ppm ("6") indicates that these PDMS moieties are in relatively uniform local environments. In addition, the well-resolved *D* ^{29}Si signal at −20.6 ppm appears at a higher frequency, compared to the PDMS ^{29}Si signal at −22.2 ppm, which is attributed to PDMS ^{29}Si atoms that experience through-space ring currents from molecularly proximate DPMS phenyl moieties ("4"). Such ring currents alter the local magnetic fields near the aromatic rings, which are only partially averaged by the restricted dynamics of the polymer chains in the cross-linked networks, consistent with the transverse ^{1}H relaxation (T_2) measurements discussed below. Notably, when comparing different foam compositions, the relative integrated ^{29}Si signal intensities of these moieties at −20.6 ppm change by a factor equal to their relative DPMS contents. For example, the relative intensity of this ^{29}Si signal for foam III synthesized with $X_{\mathrm{DPMS}} = 0.08$ (Figure 4b) is larger by a factor of 8/5 or 4, compared to foams II and I synthesized with $X_{\mathrm{DPMS}} = 0.05$ or 0.02, respectively (Figure 4c,d). This observation suggests that the DPMS side-chain groups are interacting with molecularly proximate PDMS polymer chains through phenyl ring currents, consistent with phenyl-containing organosiloxane domains that are heavily cross-linked (Figure 4a).

Quantitative comparisons of the relative populations of di- and trifunctional (*D*/*T*) ^{29}Si moieties reveal insights regarding the extent and type of PMHS cross-linking reactions. Because the initial fractions of total silanol/silane functional groups of these materials was less than unity (e.g., $\phi = 0.75$), unreacted PMHS silane groups might be expected within the foams. However, for all of the foam compositions investigated, no unreacted PMHS silane groups $(-\mathrm{O}\mathbf{Si}(\mathrm{CH_3})(\mathrm{H})\mathrm{O}-)$ were detected (typically associated with a ^{29}Si doublet at −35 and −38 ppm arising from through-bond *J*-couplings with the directly bonded proton[31]) within the sensitivity limits of the ^{29}Si NMR measurements. Water can react with a PMHS silane moiety to form a silanol group $(-\mathrm{O}-\mathbf{Si}(\mathrm{CH_3})(\mathrm{OH})-\mathrm{O}-)$ and release H_2 gas; however, no ^{29}Si signals at ca. −55 ppm from such moieties[32] were detected above the noise level. The absence of ^{29}Si signals associated with PMHS silane groups or PMHS silanol derivatives suggests that all PMHS silane groups have reacted to form trifunctional *T* ^{29}Si sites. Significantly, the fractions of the number of initial PDMS/PMHS silicon atoms in the foam resins are essentially identical to the measured fractions of integrated *D*/*T* ^{29}Si signal intensities. For the organosiloxane foams with decreasing DPMS contents of X_{DPMS}

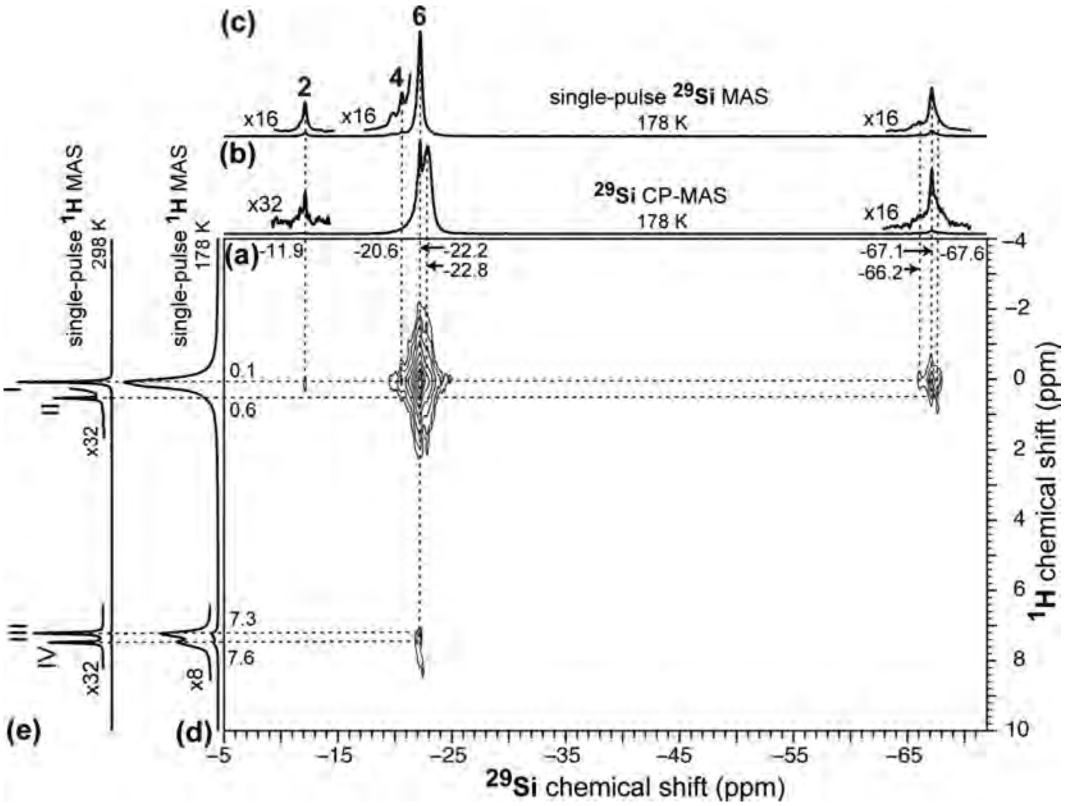

Figure 5. (a) Solid-state 2D ^{29}Si{^{1}H} HETCOR NMR spectrum of an organosiloxane foam synthesized with X_{DPMS} = 0.08 and silanol/silane fraction of ϕ = 0.75 (foam III), acquired at 178 K and 6 kHz MAS. Solid-state (b) ^{29}Si CP-MAS spectrum acquired under identical conditions as the 2D HETCOR spectrum, (c) single-pulse ^{29}Si MAS spectrum acquired at 178 K and 10 kHz MAS, (d) single-pulse ^{1}H MAS spectrum acquired at 178 K and 6 kHz MAS, and (e) single-pulse ^{1}H MAS spectrum acquired at 298 K and 60 kHz MAS.

= 0.08, 0.05, and 0.02, quantitative ^{29}Si signal analyses indicate approximately 100%, 99%, and 97% of all PMHS silane groups have reacted, respectively. To close the mass balance, it is possible that atmospheric and/or residual moisture reacted with the PMHS silane moieties in the presence of residual catalyst to form backbone silanol groups, which in turn have cross-linked with other PMHS silane groups to form *T* sites. Such reactions could occur during both the syntheses and postcure thermal treatments at 120 °C. Note that it is unlikely that scission of the organosiloxane polymer backbones has occurred to any significant extent because siloxane chain-scission mechanisms[33,34] are slow at these temperatures, compared to the time scales over which the materials were synthesized, postcured, and characterized.

Both the silanol/silane fraction ϕ and inorganic filler content also have significant influences on the bulk mechanical properties, which are correlated with their compositions and structures. These differences are elucidated by solid-state single-pulse ^{29}Si MAS NMR spectra (Supporting Information, Figure S2) acquired on foams prepared with identical DPMS contents (X_{DPMS} = 0.05), but with ϕ = 0.50 (foam IV) or with ϕ = 0.75 and including diatomaceous-earth filler (X_{diat} = 0.15, foam V). The single-pulse ^{29}Si MAS spectrum of foam IV with X_{DPMS} = 0.05 (Figure S2b) is similar to the spectrum of foam II with ϕ = 0.75 (Figure 5c and Figure S2a), with the relative integrated ^{29}Si signal intensities of the mono- (*M*), di- (*D*), and trifunctional (*T*) ^{29}Si sites differing by <5% between the two foams. Notably, this result is consistent with the quantitative analyses of *D*:*T* ^{29}Si sites discussed above, which further supports the conclusion that most or all of the PMHS silane groups have reacted to form *T* ^{29}Si sites. Thus, the key molecular differences between the foams synthesized with ϕ = 0.75 and 0.50 are (i) their relative mass fractions (0.22 vs 0.09) of low- to high-molecular-weight PDMS cross-linking sites (see Table 1), respectively, and (ii) their percentages (50% vs 25%) of PMHS silane species that have reacted with PDMS silanol moieties (a manifestation of their different ϕ values). Uniaxial compression tests (Figure 3b) establish that foams synthesized with larger silanol/silane fractions ϕ = 0.75 result in modestly (but statistically significant) stiffer materials compared to foams synthesized with ϕ = 0.50. Thus, larger mass fractions of low- to high-molecular-weight PDMS cross-linking chains and higher densities of PDMS cross-linking sites result in stiffer foams.

Likewise, the single-pulse ^{29}Si MAS NMR spectra are similar for foams synthesized with identical DPMS contents (X_{DPMS} = 0.05), but without (foam II, Figure 5c and Figure S2a) or with diatomaceous-earth filler (foam V, Figure S2c). Comparing the two spectra, the relative integrated ^{29}Si signal intensities of the mono- (*M*), di- (*D*), and trifunctional (*T*) ^{29}Si sites all differ by less than <8% between the two foams. The foam with filler particles also contains a broad, unresolved signal centered at −110 ppm from quatrafunctional Q^{4} ^{29}Si sites (^{29}Si atoms covalently bonded to four other silicon atoms through bridging oxygen atoms) associated with the siliceous diatomaceous-earth particles, which account for 7% of the total silicon atoms in the foam. Thus, single-pulse ^{29}Si MAS NMR measurements indicate that the addition of diatomaceous-earth filler particles has negligible overall influences on the local environments and compositions of the polymer chains. These results are consistent with the low specific surface area (9 m^2/g) of the filler particles, which result in sparse filler−polymer interactions. The results are also consistent with the similar dynamics of the polymer network chains in organosiloxane foams with (foam V) and without (foam II) diatomaceous-earth filler particles, as established by transverse ^{1}H NMR relaxation measurements (see below).

Molecular Structures, Interactions, and Mobilities. To measure the molecular proximities, interactions, and relative mobilities of the different organosiloxane moieties, solid-state ^{29}Si CP-MAS and 2D ^{29}Si{^{1}H} HETCOR NMR spectra were acquired on selected materials. Such measurements are sensitive to through-space ^{1}H−^{29}Si dipolar couplings that depend upon their internuclear distances and relative mobilities. At room temperature, fast molecular dynamics result in inefficient cross-polarization from ^{1}H to ^{29}Si nuclei in the elastomeric foams. At lower temperatures (e.g., just above the glass transition temperature, T_g), the dynamics of the polymer chains and side-chain groups are reduced, thereby increasing the efficiency of through-space ^{1}H−^{29}Si magnetization transfer. At 168 K, the solid-state single-pulse ^{1}H MAS spectra of the foams broaden into an unresolved distribution of signals, consistent with the foams being below T_g. Accordingly, solid-state ^{29}Si CP-MAS and 2D ^{29}Si{^{1}H} HETCOR spectra were acquired at 178 K, which is slightly above T_g, and at 215 K, which is well above T_g though sufficiently low to permit ^{1}H−^{29}Si cross-polarization. Such variable-temperature NMR measurements allow local molecular structures, through-space interactions, and relative mobilities to be probed over a range of conditions, from nearly frozen (178 K) to more mobile and elastomeric (215 K).

Measurements of the molecular-level structures and interactions between specific organosiloxane moieties slightly above T_g corroborate the ^{29}Si and ^{1}H signal assignments (Figure 4) and yield insights into the interactions that constrain the polymer networks and hence affect the macroscopic mechanical properties of the foams. For example, for an organosiloxane foam synthesized with X_{DPMS} = 0.08 and a silanol/silane fraction of ϕ = 0.75 (foam III), a solid-state 2D ^{29}Si{^{1}H} HETCOR NMR spectrum (Figure 5a) acquired at 178 K exhibits correlated 2D signal intensities that provide direct evidence of interactions between specific organosiloxane moieties. As expected, strong correlated 2D signal intensity is present at −22.2 ppm in the ^{29}Si dimension and at 0.1 ppm in the ^{1}H dimension, associated with PDMS ^{29}Si moieties ("6" in Figure 4a) and protons on their covalently bonded methyl groups ("I"). Similarly, broad correlated 2D intensity is observed at −22.8 ppm (^{29}Si) and at 0.1 ppm (^{1}H), likely associated with entangled PDMS moieties and their methyl protons. Notably, correlated signals are also observed at −22.2 ppm in the ^{29}Si dimension from PDMS ^{29}Si moieties ("6") and at 7.3 ("III") and 7.6 ppm ("IV") in the ^{1}H dimension from DPMS phenyl protons, establishing that PDMS chains are in close molecular proximities to and interacting with DPMS side-chain groups. Such interactions are confirmed by the weak, though significant, intensity correlation associated with the DPMS ^{29}Si species at −11.9 ppm and the PDMS alkyl protons at 0.1 ppm. A partially resolved 2D intensity correlation is also present at −20.6 ppm (^{29}Si) and at 0.1 ppm (^{1}H), reflecting interactions between the PDMS ^{29}Si moieties ("4") that experience DPMS phenyl ring currents and PDMS alkyl protons. Strong correlated 2D signal intensity exists between ^{29}Si signals associated with trifunctional T ^{29}Si sites on the phenyl-containing organosiloxane backbone at −66.2, −67.1, and −67.6 ppm and the ^{1}H signal from PDMS $-CH_3$ protons at 0.1 ppm ("I"). Note that the alkyl $-CH_3$ protons on the phenyl-containing organosiloxane backbone (initially associated with PMHS moieties) also contribute to signal intensity at 0.1 ppm but account for <4% of the total methyl protons associated with this ^{1}H signal. Thus, the PDMS chains interact not only with the DPMS side-chain moieties but also with the phenyl-containing organosiloxane backbone. Such interactions are readily observed near T_g and are significant because they increase the number of physical interactions that constrain the polymer network and thus may affect the bulk mechanical properties. Weak 2D correlated signal intensity also exists between T ^{29}Si sites at −67.1 and 67.6 ppm and the DPMS $-CH_3$ protons at 0.6 ppm ("II"), suggesting that these ^{29}Si moieties are associated with DPMS side-chain groups. Thus, the solid-state 2D ^{29}Si{^{1}H} HETCOR spectrum acquired at 178 K establishes the molecular compositions and structures within the organosiloxane foam that corroborate the ^{29}Si and ^{1}H chemical shift assignments in Figure 4 and provides direct molecular evidence of interactions between PDMS chains and the phenyl-containing organosiloxane moieties near T_g.

A solid-state ^{29}Si{^{1}H} CP-MAS spectrum (Figure 5b) that was acquired separately under conditions identical to the 2D HETCOR spectrum establishes the dynamics of the polymer chains and DPMS side-chain moieties slightly above T_g. Comparison of this spectrum to the quantitative single-pulse ^{29}Si MAS spectrum acquired at 178 K (Figure 5c) shows that a broad and intense ^{29}Si signal is observed at −22.8 ppm under CP-MAS conditions. This signal is likely associated with entangled PDMS polymer chains, which just above T_g, experience relatively slow molecular motions that result in strong ^{1}H−^{29}Si dipolar couplings and thus efficient ^{1}H−^{29}Si cross-polarization between entangled PDMS moieties. In addition, the monofunctional M ^{29}Si sites at ca. −12 ppm that are associated with DPMS moieties exhibit greatly reduced relative intensity under CP-MAS conditions, compared to the single-pulse ^{29}Si MAS spectrum, consistent with high DPMS mobilities, even at 178 K. The ^{29}Si CP-MAS spectrum thus establishes that PDMS and DPMS moieties exhibit relatively slow and fast segmental dynamics at 178 K, respectively.

Solid-state single-pulse ^{1}H MAS NMR spectra elucidate the relative populations and dynamics of the various proton moieties. The single-pulse ^{1}H MAS spectrum shown in Figure 5d, acquired at 178 K and 6 kHz MAS, shows a broad and intense signal at 0.1 ppm and two partially resolved signals at 7.3 and 7.6 ppm. A single-pulse ^{1}H MAS spectrum acquired on the same sample but, at 298 K and under conditions of ultrafast MAS (60 kHz), resulted in significantly increased ^{1}H resolution (Figure 5e). Both of the single-pulse ^{1}H MAS spectra in Figure 5d,e are quantitative and consistent, with their integrated ^{1}H signals accurately representing the relative populations of the different proton moieties in the foam. The spectrum at 178 K exhibits reduced ^{1}H resolution that reflects reduced mobilities of the organosiloxane networks just above T_g. In Figure 5e, well-resolved ^{1}H resonances are observed at 0.1, 0.6, 7.3, and 7.6 ppm, which are associated with the alkyl $-CH_3$ protons on the PDMS chains (>96%) and the phenyl-containing organosiloxane backbone (<4%), the alkyl $-CH_3$ DPMS protons, the *meta-/para*-protons on the DPMS aromatic rings, aromatic *ortho*-protons, respectively, corresponding to ^{1}H moieties "I", "II", "III", and "IV" in Figure 4a. The integrated intensities of the ^{1}H alkyl signals at 0.6 ppm and aromatic signals at 7.3 and

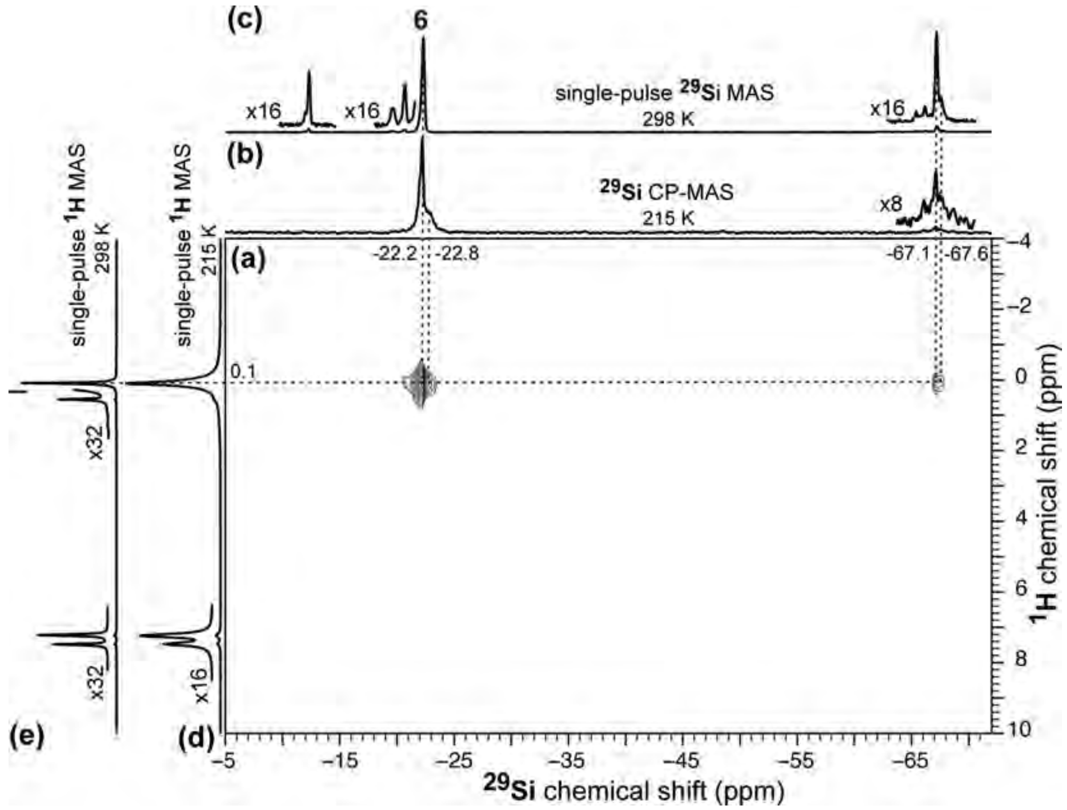

Figure 6. (a) Solid-state 2D ^{29}Si{^{1}H} HETCOR NMR spectrum of an organosiloxane foam synthesized with $X_{\mathrm{DPMS}} = 0.08$ and silanol/silane fraction of $\phi = 0.75$ (foam III), acquired at 215 K and 6 kHz MAS. Solid-state (b) ^{29}Si CP-MAS spectrum acquired under identical conditions as the 2D HETCOR spectrum, (c) single-pulse ^{29}Si MAS spectrum acquired at 298 K and 10 kHz MAS, (d) single-pulse ^{1}H MAS spectrum acquired at 215 K and 6 kHz MAS, and (e) single-pulse ^{1}H MAS spectrum acquired at 298 K and 60 kHz MAS.

7.6 ppm are each factors of approximately 8/5 or 4 greater than corresponding signals in the single-pulse ^{1}H MAS spectra for similar foams synthesized with $X_{\mathrm{DPMS}} = 0.05$ or $X_{\mathrm{DPMS}} = 0.02$, respectively, confirming that these three signals are due to DPMS moieties. Furthermore, the aromatic proton signals at 7.3 and 7.6 ppm have relative integrated signal intensities of 3:2, consistent with their assignments to the *meta-/para-* and *ortho*-protons, respectively, on the DPMS moieties. Thus, the relative populations of the DPMS proton moieties corroborate their ^{1}H signal assignments, and the dynamics of the proton moieties are consistent with their expected molecular mobilities at the acquired temperatures.

To elucidate interactions between the PDMS chains and the phenyl-containing organosiloxane moieties well above T_g, a 2D solid-state ^{29}Si{^{1}H} HETCOR spectrum of the same foam examined in Figure 5a was acquired at 215 K (Figure 6a). Understanding such interactions at higher temperatures yields insights into the network architectures of the foams when the polymer chains are mobile and elastomeric. A ^{29}Si{^{1}H} CP-MAS spectrum (Figure 6b), acquired separately under conditions identical to the 2D HETCOR spectrum, exhibits differences compared to the otherwise identical spectrum acquired at 178 K (Figure 5b) that are consistent with significantly more mobile organosiloxane species. The absence of the ^{29}Si signal at ca. −12 ppm, associated with DPMS moieties, reflects their greater dynamics at 215 K. Similarly, the ^{29}Si CP-MAS signal at −22.8 ppm associated with entangled PDMS chains is weaker, consistent with their faster molecular motions and weaker dipolar couplings. The single-pulse ^{1}H MAS spectrum shown in Figure 6d, which was also acquired at 215 K, shows a significant increase in resolution of the aromatic proton signals, compared to the otherwise identical spectrum acquired at 178 K (Figure 5d). This observation is consistent with the increased mobilities of the DPMS side-chain groups at these temperatures. The ^{29}Si CP-MAS and single-pulse ^{1}H MAS spectra thus establish the high molecular mobilities of the organosiloxane moieties at 215 K.

Nevertheless, the PDMS chains and the phenyl-containing organosiloxane backbones appear to interact strongly at 215 K, despite their high mobilities well above T_g. As shown in the 2D ^{29}Si{^{1}H} HETCOR spectrum in Figure 6a, strong 2D intensity correlations exist between ^{29}Si signals at −22.2 and −22.8 ppm, associated with unentangled ("6" in Figure 4a) and entangled PDMS moieties, respectively, and their respective alkyl ^{1}H signals at 0.1 ppm ("I"). Significantly, 2D intensity correlations are also clearly observed between ^{29}Si signals at −67.1 and 67.6 ppm associated with trifunctional *T* sites and ^{1}H signals at 0.1 ppm predominantly associated with PDMS methyl protons (>96%), suggesting interactions between PDMS chains and the phenyl-rich organosiloxane backbone. Compared to the otherwise identical spectrum acquired at 178 K in Figure 5a, the spectrum at 215 K exhibits significant differences in correlated 2D signal intensity that also reflect the higher mobilities of the elastomeric network. For example, there are no 2D intensity correlations between PDMS ^{29}Si signals at −22.0 ppm and DPMS aromatic ^{1}H signals at 7.3 and 7.6 ppm, consistent with the high mobilities of the DPMS side-chain groups at 215 K. The 2D ^{29}Si{^{1}H} HETCOR spectrum at 215 K thus suggests interactions between the cross-linking PDMS chains and the phenyl-containing organosiloxane backbone well above T_g, indicating that interactions between unentangled chains may contribute to framework mechanical properties, in addition to covalent cross-links and physical entanglements between chains.

Polymer Chain Dynamics. Differences in polymer chain dynamics can be probed by using transverse ^{1}H NMR relaxation measurements, which are sensitive to the different motional processes of the chain segments. For the elastomeric organosiloxane foams, the transverse ^{1}H relaxation times are dominated by dipole−dipole interactions between proton spins that fluctuate stochastically as the polymer chains undergo thermal motions.[35] Because of the presence of network constraints (e.g., chemical cross-links or physical entanglements) that restrict the mobilities of the polymer chains, different ^{1}H nuclei on otherwise chemically identical moieties of the polymer chains can undergo different motional processes and exhibit different NMR relaxation behaviors. For example, the restricted mobilities of polymer chains between network constraints can result in anisotropic dynamics that reduce motional averaging of the spatially dependent dipole−dipole interactions between ^{1}H nuclei and result in faster decay of transverse ^{1}H magnetization.[36] Partial averaging of the ^{1}H dipolar couplings results in residual dipolar couplings that can result in a mixed solid-like (Gaussian) and liquid-like (exponential) relaxation behavior.[36] Greater densities of network constraints are expected to result in more restricted mobilities of the polymer chain segments and, accordingly, faster relaxation of transverse ^{1}H magnetization.

Transverse ^{1}H NMR relaxation measurements using the Hahn spin−echo pulse sequence have been widely used in the literature to characterize the network structures of elastomers, resulting in correlations between the transverse T_2 relaxation times and network characteristics such as mean cross-link densities and/or network heterogeneities[29,37−42] and the fractions of network defects.[37−39,41−46] ^{1}H multiple-quantum (MQ) NMR measurements have also been developed (e.g., see references by Saalwächter et al.[47−51]) as a robust method to characterize polymer chain dynamics in elastomers.[43,44,46,52−56] The ^{1}H MQ experiments can offer certain additional advantages, including measurements of distributions of residual dipolar couplings, insights into dynamic order parameters, and results that may be less susceptible to fitting ambiguities.[47,50] Nevertheless, as shown below, the transverse ^{1}H NMR relaxation measurements conducted on the elastomeric organosiloxane foams provide useful insights into their network chain dynamics, yielding transverse ^{1}H T_2 relaxation times that correlate with their extents of cross-linking and macroscopic mechanical properties.

Transverse ^{1}H NMR relaxation measurements were conducted on the organosiloxane foams to understand the relationships between polymer chain dynamics, network structures, and macroscopic stiffnesses. The attenuations of transverse ^{1}H magnetization associated with the siloxane methyl protons are shown in Figure 7a for the organosiloxane foams with compositions listed in Table 1. The overall attenuation of ^{1}H magnetization reflects the weighted sums of the relaxation responses of different ^{1}H moieties, which exhibits three characteristic decays due to siloxane methyl protons associated with network chains ("N"), dangling end chains ("D"), and un-cross-linked species ("U"). The transverse ^{1}H relaxation data were fit to a triexponential model (eq 2), where the relative populations (X) and characteristic transverse relaxation times (T_2) of the different proton moieties are listed in Table 4. Their relative contributions to the overall relaxation curve are shown in Figure 7b for foam I (similar plots of foams II−V are shown in Figure S3, Supporting Information). Because of the complicated motional processes that affect transverse ^{1}H NMR relaxation, the relative ^{1}H populations of network chains, dangling end chains, and un-cross-linked species should be regarded as estimates. Interestingly, the ^{1}H moieties associated with network chains ("N") exhibited liquidlike exponential relaxation behavior, as the effects of solidlike Gaussian relaxation contributions due to residual dipolar couplings were not observed during the initial attenuation of transverse magnetization (Figure 7a, inset). This observation suggests that the residual dipolar couplings associated with the motionally restricted organosiloxane chains (i) were either too weak to induce measurable solidlike responses using the Hahn spin−echo experiment or (ii) caused the chain segments with the greatest motional restrictions, such

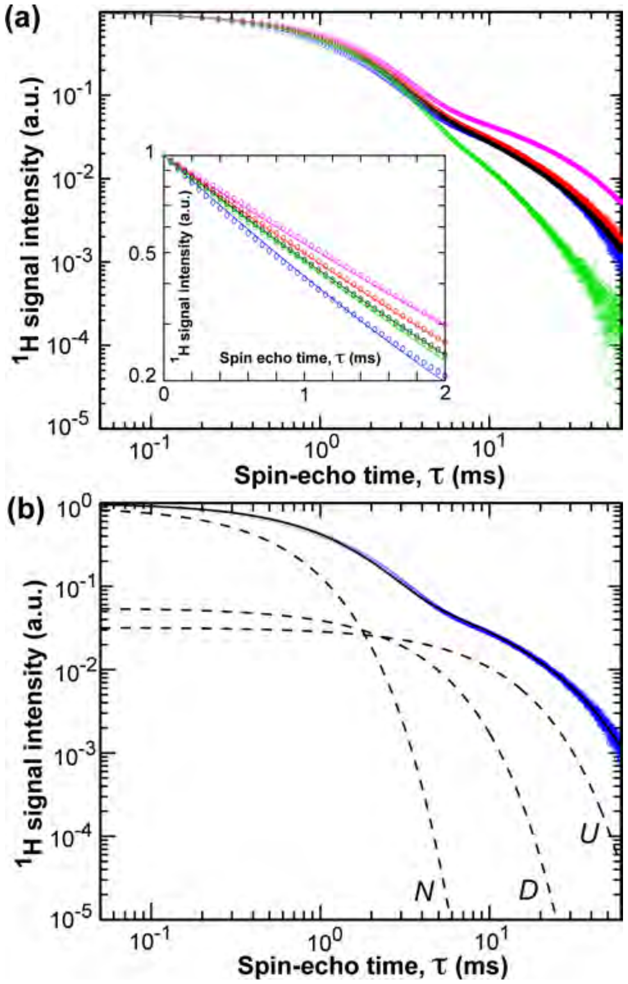

Figure 7. Transverse ^{1}H NMR relaxation measurements of the siloxane methyl protons for the different organosiloxane foams, acquired under static conditions at room temperature. (a) Log−log plots of integrated ^{1}H signal intensity vs spin−echo time τ for foams I (blue), II (black), III (magenta), IV (red), and V (green). Inset: plot of the initial attenuation of transverse ^{1}H magnetization, where solid lines represent the fit to eq 2. (b) Log−log plot of integrated ^{1}H signal intensity vs spin−echo time τ for foam I, where dashed black lines represent the contributions associated with network chains ("N"), dangling end chains ("D"), and un-cross-linked species ("U") determined from the fit to eq 2. The solid black line represents the overall fit.

Table 4. Transverse ^{1}H NMR Relaxation Properties of Elastomeric Organosiloxane Foams Synthesized with the Compositions in Table 1[a]

foams	I	II	III	IV	V
X_N	0.91	0.91	0.90	0.91	0.91
X_D	0.06	0.06	0.05	0.06	0.08
X_U	0.03	0.03	0.05	0.03	0.01
$T_{2,N}$ (ms)	1.03	1.21	1.40	1.28	1.19
$T_{2,D}$ (ms)	5.77	5.95	6.72	6.06	4.35
$T_{2,U}$ (ms)	18.1	20.7	27.5	20.9	13.9

[a] Notation: X_i, relative population of siloxane methyl protons with transverse relaxation time $T_{2,i}$; subscripts N, D, and U indicate network chains, dangling end chains, and un-cross-linked species, respectively.

as the phenyl-containing organosiloxane backbones, to relax too quickly to be detected (e.g., as measured in different polymer networks with solid-echo[29,38] or magic-sandwich echo[52,57] techniques). The ^{1}H moieties associated with both dangling end chains ("D") and un-cross-linked species ("N") exhibited liquidlike exponential relaxation responses (Figure 7b), as expected, because such ^{1}H moieties experienced isotropic motions over the time scale of the NMR experiments.

The transverse ^{1}H NMR relaxation measurements yield different relaxation times associated with network chains ($T_{2,N}$) that correlate with their macroscopic mechanical properties. For foams I, II, IV, and III without filler particles, the relative populations of siloxane methyl protons associated with network chains were essentially identical (X_N = 0.90 or 0.91), while their corresponding relaxation times varied monotonically from $T_{2,N}$ = 1.03 to 1.40 ms (Table 4). Their Young's moduli also varied monotonically from E_f = 1.00 to 0.40 kPa and from E_s = 20.9 to 8.3 kPa. Similarly, at larger strains, $\sigma_{50\%}$ varied monotonically from 24.5 to 10.6 kPa. Therefore, among the organosiloxane foams without filler particles, shorter $T_{2,N}$ relaxation times correlate with stiffer materials at both small and large strains. Foams I, II, and III exhibit increasing DPMS contents of X_{DPMS} = 0.02, 0.05, and 0.08 and decreasing extents of cross-linking (as quantitatively established by single-pulse ^{29}Si MAS NMR measurements), establishing that shorter $T_{2,N}$ relaxation times and correspondingly more restricted mobilities of network chains correlate with increasing cross-linking densities. Foams II and IV exhibit identical DPMS contents of X_{DPMS} = 0.05, but foam II exhibits modestly shorter $T_{2,N}$ relaxation times and stiffer mechanical properties, likely due to its higher mass fraction of low- (short) to low- (short) to high-molecular-weight PDMS chains. Note that during the syntheses of the organosiloxane foams concurrent cross-linking reactions and *in situ* generation of porosity due to the evolution of H_2 gas will likely stretch a fraction of the network chains, which would also lead to restricted chain mobilities and shorter transverse T_2 NMR relaxation times. Differences in ^{1}H $T_{2,N}$ relaxation times among the foams due to such effects, however, are expected to be small compared to larger differences associated with their different respective cross-linking densities.

The addition of diatomaceous-earth silica particles results in negligible differences in the transverse ^{1}H NMR relaxation times associated with network chains. When the foam with diatomaceous-earth filler (X_{diat} = 0.15, foam V) is compared to a similar foam with an identical DPMS content (X_{DPMS} = 0.05) but without filler particles (foam II), the foams exhibited identical relative populations of siloxane methyl protons associated with network chains (X_N = 0.91) and very similar $T_{2,N}$ relaxation times (1.19 and 1.21 ms for foams with and without filler, respectively). These results indicate that the polymer chains and the filler particles do not interact significantly within the sensitivity of the NMR measurements, consistent with the low specific surface area (9 m^2/g) of the diatomaceous-earth particles. Instead, the organosiloxane foams with diatomaceous-earth filler are stiffer at large strains because the inclusion of rigid filler particles in deformable polymer networks reinforces the polymer matrix when subjected to mechanical strain.[11,29,58]

The dangling end chains and un-cross-linked species are elastically ineffective and have negligible influences on the bulk mechanical responses of the organosiloxane foams. As seen in Table 4, the relative populations of dangling end chains and un-cross-linked species range from X_D = 0.05 to 0.08 and X_U = 0.01 to 0.05, respectively, and their corresponding transverse relaxation times range from $T_{2,D}$ = 4.35 to 6.72 ms and $T_{2,U}$ = 13.9 to 27.5 ms. The relative populations of the dangling end chains and un-cross-linked species are similar among the different organosiloxane foams. As expected, the dangling end chains and un-cross-linked species exhibited greater ^{1}H T_2 times compared to the network chains, as their less restricted dynamics result in enhanced motional averaging of ^{1}H−^{1}H dipole−dipole couplings and hence longer transverse relaxation times. While the dangling end chains exhibited $T_{2,D}$ relaxation times that are relatively similar, the un-cross-linked species exhibited a greater range of $T_{2,U}$ values, possibly due to different molecular weights of PDMS oligomeric compounds within the materials. Note that while ^{29}Si signals associated with cyclic D_4 PDMS species are resolved in the single-pulse ^{29}Si MAS NMR spectra ("3" in Figure 4), the ^{29}Si signals associated with cyclic D_{5+} sites are nearly indistinguishable from bulk PDMS signals at −22.2 ppm[30] ("6" in Figure 4).

CONCLUSIONS

The molecular compositions, structures, interactions, and polymer chain dynamics of elastomeric organosiloxane foams have been shown to be correlated with their macroscopic mechanical properties. Uniaxial compression measurements establish that materials with varying framework compositions exhibit significantly different mechanical properties, such as Young's moduli and extents of irreversible strain-induced softening. Quantitative analyses of MXCT images reveal that their cell microstructures (e.g., average pore sizes and distributions) are similar and cannot account for such differences, enabling microstructural contributions to the bulk mechanical properties to be distinguished from contributions associated with the foam frameworks themselves. Solid-state NMR measurements results reveal significant differences in the molecular and polymer network characteristics among the foams that are correlated with their macroscopic mechanical responses.

Elastomeric organosiloxane foams with higher extents of network cross-linking and lower concentrations of phenyl side-chain moieties are stiffer at both small and large strains, as established for the final products by quantitative single-pulse ^{29}Si NMR measurements. Network chains that exhibit more restricted mobilities, as manifested by shorter transverse ^{1}H NMR relaxation times, are correlated with stiffer materials. At temperatures just above the glass transition temperature T_g, solid-state 2D ^{29}Si{^{1}H} HETCOR NMR spectra reveal evidence of interactions between PDMS chains and the phenyl-containing organosiloxane backbones, which appear to persist even well above T_g. Such interactions may contribute to the overall mechanical properties of the organosiloxane foams, in addition to covalent chemical cross-links and physical chain entanglements. For materials without filler particles, the magnitude of irreversible strain-softening (Mullins effect) upon mechanical compression is correlated with the relative mass fractions of low- (short) to high-molecular-weight (long) PDMS chains, where a smaller fraction of short to long cross-linking chains significantly reduces this effect. These results are consistent with the strain-softening of unfilled elastomers being due to quasi-irreversible network deformations associated with extended short polymer chains. The addition of low-surface-area (9 m^2/g) diatomaceous-earth filler particles results in significantly stiffer organosiloxane foams at large strains and a greater irreversible strain-induced softening. ^{29}Si MAS and transverse ^{1}H relaxation NMR measurements establish negligible overall interactions between the vast majority of the polymer chains and filler particles, consistent with the low specific surface areas of the particles. These results highlight the predominantly physical reinforcement effects that filler particles can have on a polymer network. Collectively, the results establish that the molecular compositions, structures, interactions, and polymer chain dynamics of the organosiloxane network have strong influences on the macroscopic mechanical properties of the elastomeric foams, which may be adjusted independently of cell microstructures within synthetic limits. Such insights are expected to aid the development of rational design strategies for syntheses and processing of both cellular and noncellular elastomeric polymers for diverse mechanical applications.

■ ASSOCIATED CONTENT

Ⓢ Supporting Information

Quantitative MXCT image processing techniques; additional discussions of cell microstructures; mean 2D pore radii per MXCT image R_z and R_x, analyzed as a function of depth orthogonal to the z- and x-axes, respectively; solid-state single-pulse ^{29}Si MAS NMR spectra of foams II, IV, and V; transverse ^{1}H NMR relaxation measurements of foams II, III, IV, and V, showing the quantitative contributions of network chains, dangling end chains, and un-cross-linked species. The Supporting Information is available free of charge on the ACS Publications website at DOI: 10.1021/acs.macromol.5b00532.

■ AUTHOR INFORMATION

Corresponding Author

*E-mail: bradc@engineering.ucsb.edu (B.F.C.).

Notes

The authors declare no competing financial interest.

■ ACKNOWLEDGMENTS

The authors thank Dr. Brian Patterson, Dr. Michael Janicke, and Dr. Jerry Hu for assistance with the MXCT, solution-state NMR, and variable-temperature solid-state NMR measurements, respectively, and Prof. Moshe Gottlieb for helpful discussions that initiated these investigations. This work was supported by the U.S. Department of Energy through the Institute of Multiscale Materials Studies at Los Alamos National Laboratory and the U.S. National Science Foundation (NSF) under Grant CHE-0924654. R.J.M. acknowledges the Warren and Katharine Schlinger Foundation for a doctoral fellowship. Solid-state NMR measurements were conducted using the Material Research Laboratory Central Facilities at UCSB, which are supported by the NSF MRSEC Program under Award DMR 1121053.

■ REFERENCES

(1) Gibson, L. J.; Ashby, M. F. *Cellular Solids: Structures and Properties*, 2nd ed.; Cambridge University Press: Cambridge, 1997.

(2) Gibson, L. *Mater. Sci. Eng., A* **1989**, *110*, 1–36.

(3) Ashby, M. F. *Philos. Trans. R. Soc., A* **2006**, *364*, 15–30.

(4) Shutov, F. A. *Adv. Polym. Sci.* **1983**, *51*, 155–218.

(5) Nielsen, L. E.; Landel, R. F. *Mechanical Properties of Polymers and Composites*, 2nd ed.; Marcel Dekker, Inc.: New York, 1994.

(6) Ebewele, R. O. *Polymer Science and Technology*; CRC Press: Boca Raton, FL, 2000.

(7) Mangaraj, D. *Rubber Chem. Technol.* **2002**, *75*, 365–427.

(8) Lucas, P.; Robin, J.-J. *Adv. Polym. Sci.* **2007**, *209*, 111–147.

(9) Hamley, I. W., Ed.; *Developments in Block Copolymer Science & Technology*; John Wiley & Sons, Ltd.: Chichester, 2004.

(10) Brook, M. A. *Silicon in Organic, Organometallic, and Polymer Chemistry*; John Wiley & Sons, Inc.: New York, 2000.

(11) Bokobza, L. *Macromol. Mater. Eng.* **2004**, *289*, 607–621.

(12) Mark, J. E. *Acc. Chem. Res.* **2006**, *39*, 881–888.

(13) Patterson, B. M.; Henderson, K.; Smith, Z. *J. Mater. Sci.* **2013**, *48*, 1986–1996.

(14) Montminy, M. D.; Tannenbaum, A. R.; Macosko, C. W. *J. Colloid Interface Sci.* **2004**, *280*, 202–211.

(15) Patterson, B. M.; Hamilton, C. E. *Anal. Chem.* **2010**, *82*, 8537–8543.

(16) Fung, B. M.; Khitrin, A. K.; Ermolaev, K. *J. Magn. Reson.* **2000**, *142*, 97–101.

(17) Hediger, S.; Meier, B. H.; Kurur, N. D.; Bodenhausen, G.; Ernst, R. R. *Chem. Phys. Lett.* **1994**, *223*, 283–288.

(18) Caravatti, P.; Bodenhausen, G.; Ernst, R. *Chem. Phys. Lett.* **1982**, *89*, 363–367.

(19) Schmidt-Rohr, K.; Spiess, H. W. *Multidimensional Solid-State NMR and Polymers*; Academic Press Ltd.: San Diego, 1994.

(20) States, D. J.; Haberkorn, R. A.; Ruben, D. J. *J. Magn. Reson.* **1982**, *48*, 286–292.

(21) Rice, J. A. *Mathematical Statistics and Data Analysis*, 2nd ed.; Duxbury Press: Belmont, 1995.

(22) Ferry, J. D. *Viscoelastic Properties of Polymers*, 3rd ed.; John Wiley & Sons, Inc.: New York, 1980.

(23) Mullins, L. *Rubber Chem. Technol.* **1969**, *42*, 339–362.

(24) Diani, J.; Fayolle, B.; Gilormini, P. *Eur. Polym. J.* **2009**, *45*, 601–612.

(25) Harwood, J. A. C.; Mullins, L.; Payne, A. R. *J. Appl. Polym. Sci.* **1965**, *9*, 3011–3021.

(26) Harwood, J. A. C.; Payne, A. R. *J. Appl. Polym. Sci.* **1966**, *10*, 315–324.

(27) Harwood, J. A. C.; Payne, A. R. *J. Appl. Polym. Sci.* **1966**, *10*, 1203–1211.

(28) Roland, C. M. *Rubber Chem. Technol.* **1989**, *62*, 880–895.

(29) Litvinov, V. M.; Orza, R. A.; Klüppel, M.; van Duin, M.; Magusin, P. C. M. M. *Macromolecules* **2011**, *44*, 4887–4900.

(30) Engelhardt, G.; Jancke, H. *Polym. Bull.* **1981**, *5*, 577–584.

(31) Labouriau, A.; Stephens, T. NMR Investigations of Room Temperature Vulcanized Polysiloxane Rubbers. Los Alamos National Laboratory Tech. Report, LA-UR-05-0848, 2005.

(32) Engelhardt, G.; Jancke, H.; Lippmaa, E.; Samoson, A. *J. Organomet. Chem.* **1981**, *210*, 295–301.

(33) Camino, G.; Lomakin, S. M.; Lazzari, M. *Polymer* **2001**, *42*, 2395–2402.

(34) Camino, G.; Lomakin, S. M.; Lageard, M. *Polymer* **2002**, *43*, 2011–2015.

(35) Levitt, M. H. *Spin Dynamics: Basics of Nuclear Magnetic Resonance*, 2nd ed.; John Wiley & Sons, Ltd.: Chichester, West Sussex, 2008.

(36) Cohen-Addad, J. *Prog. Nucl. Magn. Reson. Spectrosc.* **1993**, *25*, 1−316.
(37) Orza, R. A.; Magusin, P. C. M. M.; Litvinov, V. M.; van Duin, M.; Michels, M. A. J. *Macromolecules* **2007**, *40*, 8999−9008.
(38) Litvinov, V. M. *Macromolecules* **2006**, *39*, 8727−8741.
(39) Litvinov, V. M.; Dias, A. A. *Macromolecules* **2001**, *34*, 4051−4060.
(40) Agarwal, V.; van Erp, T. B.; Balzano, L.; Gahleitner, M.; Parkinson, M.; Govaert, L. E.; Litvinov, V.; Kentgens, A. P. *Polymer* **2014**, *55*, 896−905.
(41) Simon, G.; Baumann, K.; Gronski, W. *Macromolecules* **1992**, *25*, 3624−3628.
(42) Andreis, M.; Koenig, J. *Adv. Polym. Sci.* **1989**, *89*, 69−160.
(43) Gjersing, E.; Chinn, S.; Giuliani, J. R.; Herberg, J.; Maxwell, R. S.; Eastwood, E.; Bowen, D.; Stephens, T. *Macromolecules* **2007**, *40*, 4953−4962.
(44) Chinn, S. C.; Alviso, C. T.; Berman, E. S. F.; Harvey, C. A.; Maxwell, R. S.; Wilson, T. S.; Cohenour, R.; Saalwächter, K.; Chassé, W. *J. Phys. Chem. B* **2010**, *114*, 9729−9736.
(45) Mayer, B. P.; Reimer, J. A.; Maxwell, R. S. *Macromolecules* **2008**, *41*, 1323−1327.
(46) Maxwell, R. S.; Chinn, S. C.; Solyom, D.; Cohenour, R. *Macromolecules* **2005**, *38*, 7026−7032.
(47) Saalwächter, K. *Prog. Nucl. Magn. Reson. Spectrosc.* **2007**, *51*, 1−35.
(48) Saalwächter, K.; Ziegler, P.; Spyckerelle, O.; Haidar, B.; Vidal, A.; Sommer, J.-U. *J. Chem. Phys.* **2003**, *119*, 3468−3482.
(49) Saalwächter, K. *J. Chem. Phys.* **2004**, *120*, 454−464.
(50) Saalwächter, K. *Macromolecules* **2005**, *38*, 1508−1512.
(51) Vaca Chávez, F.; Saalwächter, K. *Macromolecules* **2011**, *44*, 1549−1559.
(52) Papon, A.; Saalwächter, K.; Schäler, K.; Guy, L.; Lequeux, F.; Montes, H. *Macromolecules* **2011**, *44*, 913−922.
(53) Mayer, B. P.; Lewicki, J. P.; Weisgraber, T. H.; Small, W.; Chinn, S. C.; Maxwell, R. S. *Macromolecules* **2011**, *44*, 8106−8115.
(54) Vieyres, A.; Pérez-Aparicio, R.; Albouy, P.-A.; Sanseau, O.; Saalwächter, K.; Long, D. R.; Sotta, P. *Macromolecules* **2013**, *46*, 889−899.
(55) Schlögl, S.; Trutschel, M.-L.; Chassé, W.; Riess, G.; Saalwächter, K. *Macromolecules* **2014**, *47*, 2759−2773.
(56) Saleesung, T.; Reichert, D.; Saalwächter, K.; Sirisinha, C. *Polymer* **2015**, *56*, 309−317.
(57) Maus, A.; Hertlein, C.; Saalwächter, K. *Macromol. Chem. Phys.* **2006**, *207*, 1150−1158.
(58) Guth, E.; Gold, O. *Phys. Rev.* **1938**, *53*, 322.

SUPPORTING INFORMATION:

Molecular Origins of Macroscopic Mechanical Properties of Elastomeric Organosiloxane Foams

R. J. Messinger,[†] T. G. Marks,[‡] S. S. Gleiman,[¶] F. Milstein,[‡] and B. F. Chmelka[*],

Department of Chemical Engineering, University of California, Santa Barbara, California 93106 U.S.A., Department of Mechanical Engineering, University of California, Santa Barbara, California 93106 U.S.A., and Institute of Multiscale Materials Studies, Los Alamos National Laboratory, Los Alamos, New Mexico 87544 U.S.A.

E-mail: bradc@engineering.ucsb.edu

Quantitative MXCT image processing techniques. Pore sizes and distributions were quantitatively analyzed using a custom image analysis program specifically designed to identify structural features from a series of 2D MXCT images. The image analysis program was written in C++ and loaded each 2D MXCT image sequentially via the program *ImageMagick*.™ The 2D MXCT slices were loaded as grayscale bit images, such that each pixel carried only intensity information, varying from black (void space) to white (polymer framework), respectively. To save computation time, to avoid edge effects, and to facilitate 3D image processing, each 2D image was cropped to an identical 2D sub-area, collectively forming a 3D volume-of-interest. Before extraction of microstructural parameters, each image was smoothed using a localized Gaussian mask, which is a low-pass filter that reduces noise from the X-ray reconstruction process. The smoothed images

---

[*] To whom correspondence should be addressed

[†] UCSB Chemical Engineering

[‡] UCSB Mechanical Engineering

[¶] Los Alamos National Laboratory

were then converted to binary images by assigning either an 'on' (white) or 'off' (black) value to each pixel, depending on the intensity of the pixel compared to a threshold value. Otsu's method (Otsu, N. *IEEE T. Syst. Man Cyb.*, **1979**, *9*, 62-66) for shape-based image thresholding of the normalized gray level histogram was used to determine the optimum threshold value. Each 2D binary image was analyzed to determine microstructural features of interest, such as the edges, locations, and sizes of 2D pores. Pore surfaces, which are represented by edges in the 2D images, were found by using the Canny edge-detection method (Canny, J. *IEEE T. Pattern Anal.*, **1986**, *8*, 679-698). Pore sizes and locations were established by using a Hough transform (Duda, R.O.; Hart, P.E. *Commun. ACM*, **1972**, *15*, 11-15), a feature extraction technique used to find objects that exhibit specific classes of shapes (e.g., circular objects). The Hough transform was used to identify 2D pores by surveying edge pixels for the location and radii of best-fit circles. To compute 3D pore radii and their distributions, best-fit circles from a series of consecutive 2D MXCT images were grouped together by location and collectively used to estimate the center, radii, and total number of all 3D pores within the volume-of-interest, according to best-fit spheres. The probability density functions of 3D pore radii were determined by normalizing a histogram of 3D pore radii with a bin size of 20 μm. To calculate the radial distribution functions, the number of 3D pore centers located within a differential spherical shell dr thick (24.20 μm) was evaluated as a function of the radial distance r from a given pore, divided by the shell volume, and then normalized by the bulk number density of 3D pores. This procedure was repeated for each 3D pore and subsequently averaged.

Additional discussions of cell microstructures. Organosiloxane foams I, II, and IV have very similar cell microstructures, even though they have different DPMS contents (X_{DPMS} = 0.02 or 0.05) and silanol/silane fractions (ϕ = 0.50 or 0.75). The bulk-averaged 2D pore radii for these materials are nearly identical, with $\bar{R}_z = 154, 157$, and 160 μm and corresponding standard deviations of $\sigma_{R,z} = 15, 11$, and 15 μm for foams I, II, and IV, respectively, and similarly $\bar{R}_x = 149, 154$, and 152 μm with $\sigma_{R,x} = 6, 6$, and 8 μm. Their probability distribution functions of 3D pore radii (Figure 2a,b) are also very similar, and consequently the bulk-averaged 3D pore radii are nearly identical: $\bar{P}_z = 134, 136$, and 142 μm with standard deviations of their size distributions $\sigma_{P,z}$ = 80, 87, and 86 μm, for foams I, II, and IV, respectively, and $\bar{P}_x = 133, 131$, and 137 μm with $\sigma_{P,x} = 80, 85$, and 81 μm. In addition, the radial distribution functions of 3D pore locations (Figure 2c,d) are very similar. These functions exhibit a weak maximum (ca. 350-400 μm) and minimum (ca. 600 μm), indicating a weak degree of local structural order that reflects the characteristic dimensions of the 3D pore radii. For example, the location of the maximum is approximately equal to the length of two average pore radii (ca. 135 μm each) and the framework material between them, suggesting an average width of ca. 100 μm for the organosiloxane framework separating two pores. Thus, comparisons among foams I, II, and IV indicate that they have very similar cell microstructures, as established by their mean 2D and 3D pore dimensions, pore size distributions of 3D pore radii, and radial distribution functions of 3D pore locations.

By comparison, foams III and V have modestly larger pore dimensions though otherwise share similar microstructural characteristics compared to foams I, II, and IV. When analyzed orthogonal to the x-axis, foam III has essentially identical mean 2D pore radii per MXCT image (R_x, Figure S1b) and bulk-averaged 2D pore radii ($\bar{R}_x = 152$ μm with $\sigma_x = 10$ μm), but exhibits larger pore sizes with respect to the z-axis ($\bar{R}_z = 195$ μm with $\sigma_z = 15$ μm). Spherical approximations of the modestly anisotropic pore shapes result in probability distribution functions of 3D pore radii (Figure 2a,b) that yield bulk-averaged 3D pore radii $\bar{P}_z = 175$ μm with $\sigma_{P,z} = 104$ μm and $\bar{P}_x = 177$ μm with $\sigma_{P,x} = 109$ μm. The radial distribution functions of 3D pore locations (Figure 2c,d) exhibit higher noise levels compared to foams I, II, and IV, which is likely a consequence of the larger standard deviations of 3D pore radii ($\sigma_{P,z}$ and $\sigma_{P,x}$). Foam V also exhibits modestly larger pore dimensions compared to foams I, II, and IV, though unlike foam III has spherical pore shapes. Specifically, foam V has bulk-averaged 2D pore radii of $\bar{R}_z = 205$ μm with $\sigma_z = 15$ μm and $\bar{R}_x = 216$ μm with $\sigma_x = 19$ μm, when analyzed orthogonal to the z- and x-axes, respectively. The probability distribution functions of 3D pore radii (Figure 2a,b) are comparable to foams I, II, and IV, yielding bulk-averaged 3D pore radii of $\bar{P}_z = 154$ μm with $\sigma_{P,z}$ = 121 μm and $\bar{P}_x = 165$ μm with $\sigma_{P,x} = 130$ μm. Thus, $\bar{P}_z$ and $\bar{P}_x$ are ca. 20 μm and 30 μm larger, respectively, compared to foams I, II, and IV. Note that the modestly larger bulk-averaged 3D pore radii (20–30 μm) are expected to be more accurate measurements compared to the larger bulk-averaged 2D pore radii (50 to 60 μm), because 2D analyses overestimate the sizes of larger pores due to their presence in larger numbers of consecutive 2D MXCT images. The radial distribution functions of 3D pore locations (Figure 2c,d) of foam V exhibit higher noise levels compared to foams I, II, and IV due to the larger standard deviations of 3D pore radii ($\sigma_{P,z}$ and $\sigma_{P,x}$).

The modestly larger pore sizes of foams III and V are consequences of the compositions of their respective resin mixtures. For foam III, the moderately larger pore dimensions orthogonal to the z-axis are likely a result of the high DPMS content ($X_{DPMS} = 0.08$) in its resin. Because the reaction kinetics between DPMS and PMHS occur at a faster rate relative to the cross-linking reaction between PDMS and PMHS, generation of H_2 gas and subsequent bubble formation are expected to occur to a somewhat great extent before the cross-linking reactions impart sufficient mechanical stability to the framework. Because gravity is parallel to the z-axis during syntheses of the foams, the viscous resin likely drains slightly before solidifying, resulting in larger pore dimensions orthogonal to the z-axis, but not the x-axis. For foam V, the larger pore sizes are a result of diatomaceous-earth-filler particles ($X_{diat} = 0.15$) within the resin mixture. The diatomaceous-earth particles not only increase the viscosity of the resin, but also may promote the coalescence of adjacent H_2 bubbles by destabilizing the thin films between them (note that the average particle size is 8 μm, which is small but nontrivial compared to the width of framework material between pores). An enhanced rate of bubble coalescence would thus result in an organosiloxane foam with larger pore sizes, as observed for foam V.

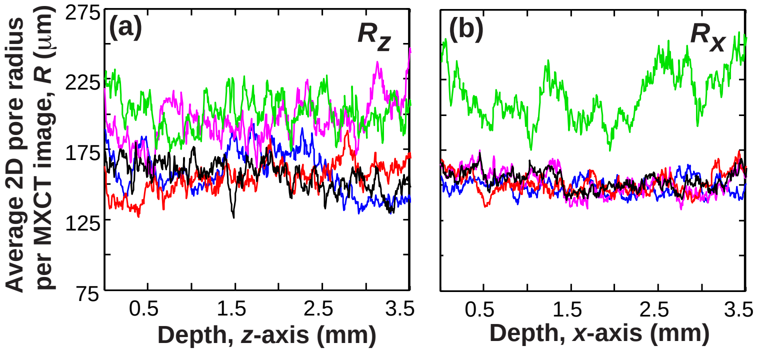

Figure S1: Mean 2D pore radii per MXCT image (a) R_z and (b) R_x analyzed as a function of depth orthogonal to the z- and x-axes, respectively, for foams I (blue), II (black), III (magenta), IV (red), and V (green). The bulk-averaged 2D pore radii $\bar{R}_z$ and $\bar{R}_x$ and their associated standard deviations $\sigma_{R,z}$ and $\sigma_{R,x}$ are listed in Table 2 in the main article.

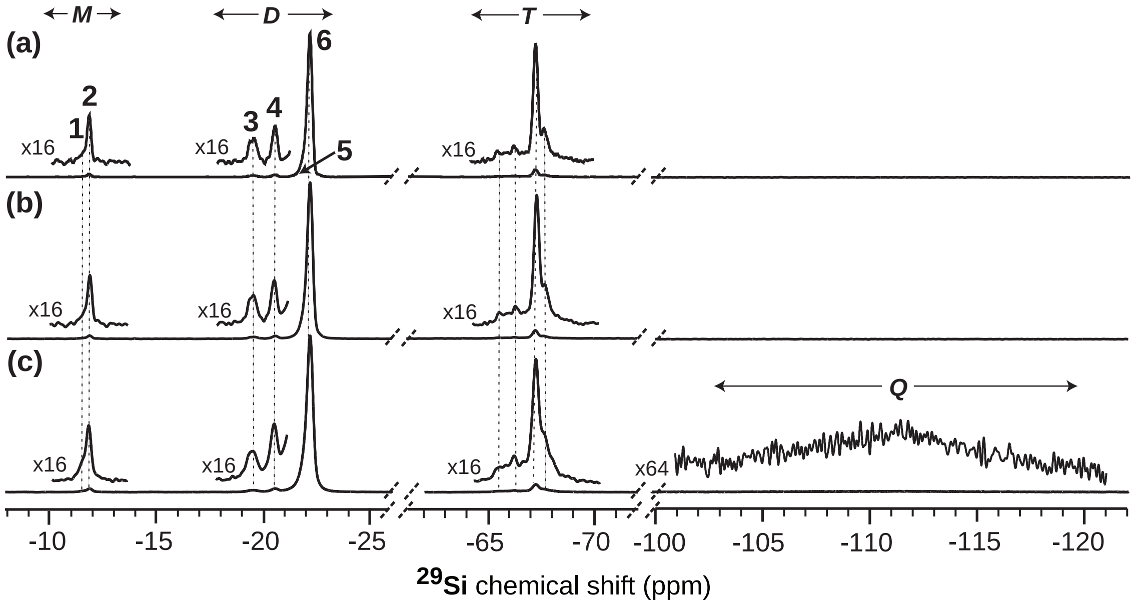

Figure S2: Solid-state single-pulse ^{29}Si MAS NMR spectra acquired for organosiloxane foams synthesized with identical DPMS contents ($X_{DPMS} = 0.05$), but different silanol/silane fractions (ϕ) and/or filler contents: (a) $\phi = 0.75$, (b) $\phi = 0.50$, and (c) $\phi = 0.75$ with diatomaceous-earth filler ($X_{diat} = 0.15$), corresponding to foams II, IV, and V, respectively. All spectra were acquired at 10 kHz MAS under ambient conditions. NMR chemical shift assignments for ^{29}Si moieties correspond to those in Figure 4a, with regions of the spectra corresponding to the M, D, T and Q ^{29}Si species labeled as shown.

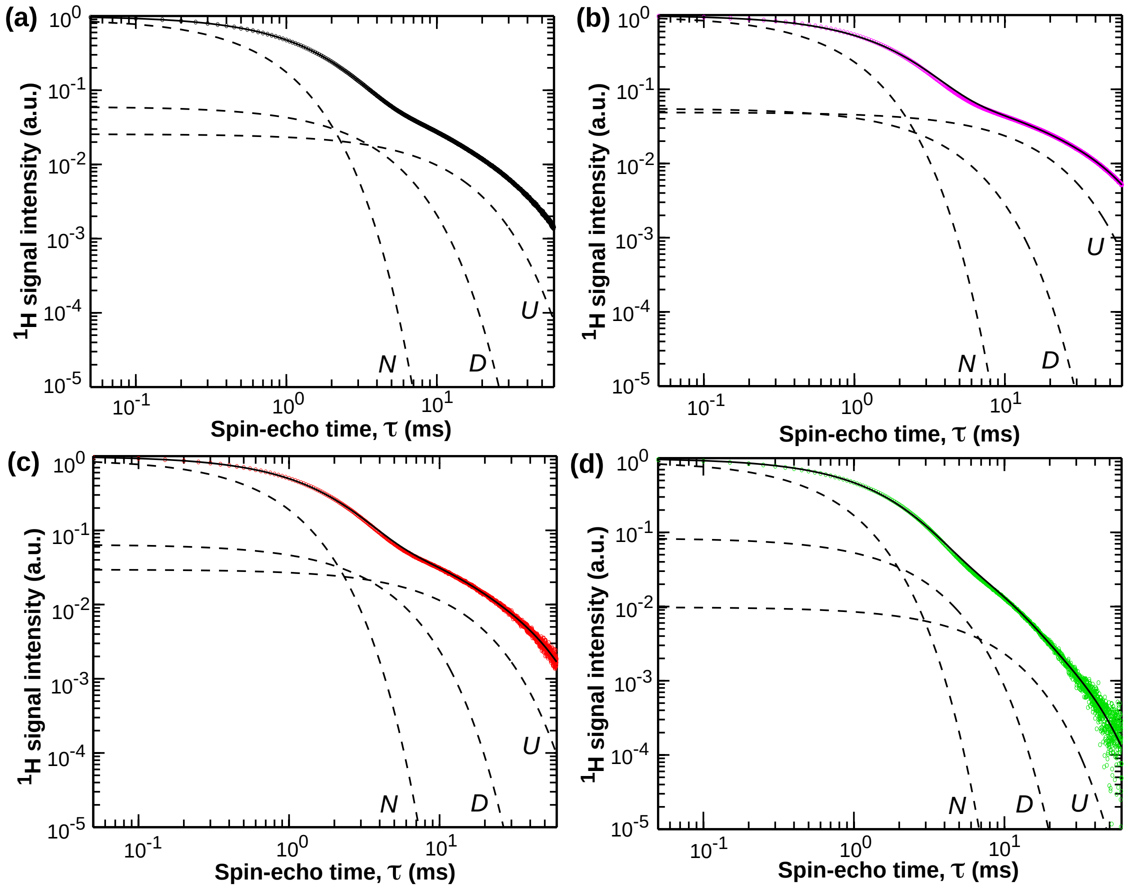

Figure S3: Transverse ^{1}H NMR relaxation measurements of the siloxane methyl protons for the different organosiloxane foams, acquired under static conditions at room temperature. (a) Log-log plots of integrated ^{1}H signal intensity vs. spin-echo time τ for foams (a) II, (b) III, (c) IV, and (d) V, where dashed black lines represent the contributions associated with network chains (*N*'), dangling end chains ('*D*'), and uncross-linked species ('*U*'). The solid black lines represent the overall fits to the data. The corresponding populations and transverse T_2 relaxation times for each of the different components are listed in Table 4 in the main article.